Effect of Microstructural Interfaces on the Mechanical Response of Crystalline Metallic Materials

Thesis by

Zachary H. Aitken

In Partial Fulfillment of the Requirement for the

degree of

Doctor of Philosophy

CALIFORNIA INSTITUTE OF TECHNOLOGY

Pasadena, California

2015

(Defended May 14, 2015)

Acknowledgements

I'd like to thank my adviser, Julia R. Greer, for her support throughout my time at Caltech. I have learned so much from her, becoming a better researcher and communicator. It is because of her support that I have had so many opportunities throughout my PhD program. I also thank her for her support through NSF CAREER Grant (DMR-0748267) which made much of this research possible.

Thank you to all the members of the Greer group (past and present, too many to list). Their friendliness and sociability makes all the difference. Especially to all my office mates, Andrew, Shelby, Joanna, David, Viki and Rachel who always made our office a fun place to be.

I'd like to thank the staff of the Kavli Nanoscience Institute and Carol Garland for TEM help. Carol was always available for discussion and was a deep source of knowledge on microscopy.

Thanks to all the enthusiastic undergraduate and high-school students that I've had for the opportunity to work with. I wish Justin, Amal, Andy, Mitchell, David, and Stephanie the best of luck in their future careers.

I'm grateful for all the friends I've made through numerous collaborations and look forward to working with them in the future. I'm grateful to Chris and Garritt for all they've taught me and for all their help and patience throughout my PhD career.

I'd like to thank my family, whose constant love and support I have always been able to count on.

Abstract

Advances in nano-scale mechanical testing have brought about progress in the understanding of physical phenomena in materials and a measure of control in the fabrication of novel materials. In contrast to bulk materials that display size-invariant mechanical properties, sub-micron metallic samples show a critical dependence on sample size. The strength of nano-scale single crystalline metals is well-described by a power-law function, $\sigma \propto D^{-n}$, where *D* is a critical sample size and *n* is a experimentally-fit positive exponent. This relationship is attributed to source-driven plasticity and demonstrates a strengthening as the decreasing sample size begins to limit the size and number of dislocation sources. A full understanding of this size-dependence is complicated by the presence of microstructural features such as interfaces that can compete with the dominant dislocation-based deformation mechanisms. In this thesis, the effects of microstructural features such as grain boundaries and anisotropic crystallinity on nano-scale metals are investigated through uniaxial compression testing. We find that nano-sized Cu covered by a hard coating displays a Bauschinger effect and the emergence of this behavior can be explained through a simple dislocation-based analytic model. Al nano-pillars containing a single vertically-oriented coincident site lattice grain boundary are found to show similar deformation to single-crystalline nano-pillars with slip traces passing through the grain boundary. With increasing tilt angle of the grain boundary from the pillar axis, we observe a transition from dislocation-dominated deformation to grain boundary sliding. Crystallites are observed to shear along the grain boundary and molecular dynamics simulations reveal a mechanism of atomic migration that accommodates boundary sliding. We conclude with an analysis of the effects of inherent crystal anisotropy and alloying on the mechanical behavior of the Mg alloy, AZ31. Through comparison to pure Mg, we show that the size effect dominates the strength of samples below 10 µm, that differences in the size effect between hexagonal slip systems is due to the inherent crystal anisotropy, suggesting that the fundamental mechanism of the size effect in these slip systems is the same.

Table of Contents

List of Figures and Tables

1. Introduction

1.1 Mechanics of crystalline metals

Mechanical properties of materials such as strength, ductility and stiffness are determined by their microstructure. In homogeneous crystalline metals, microstructure can largely be described by defects such as dislocations and grain boundaries. In heterogeneous crystalline metals, this can also include substitution or interstitial atoms (point defects) as well as phase boundaries. Dislocations are line defects that delineate regions of defected crystal. About these lines, the local lattice is displaced from its ideal configuration and motion of a dislocation involves localized atomic bond breaking along the dislocation line and along a crystalline slip plane. Dislocation glide through a crystal acts as the carrier of plasticity and accommodates deformation and stress relaxation. The force required to move dislocations, and the nucleation of new dislocations, as well as the interactions between dislocations, characterize the strength and post-elastic behavior of a crystalline metal.

A crystal defines a region of local atomic order and bulk metals are typically composed of several crystalline domains, referred to as grains, and the interfaces between domains, referred to as grain boundaries in homogeneous materials. In multi-phase materials, interfaces can also include boundaries between internal phases or between a bulk material and an applied coating. The importance of interfaces in the mechanical behavior of metals is seen in the interactions between interfaces and dislocations. Hard precipitates can serve to block dislocation motion through the matrix and the local stresses at the interface between the precipitate and the matrix can in turn serve as a source of dislocations. The interaction between dislocations and grain boundaries is well-demonstrated by the Hall-Petch relation, $\sigma \propto \frac{1}{\sqrt{d}}$, where σ is the strength and d is the grain size [1]. This dependence arises by the mechanism of dislocation pile-ups at the grain boundary and is observed to apply to grain sizes down to 10-25 nm. The back-stresses generated by the accumulation of dislocations at the grain boundary require higher stresses for dislocation movement and activation of dislocation sources. Grain boundaries can also contribute to plastic deformation through grain boundary sliding, where one crystallite translates relative to the other. In the case of materials with grain sizes below 10-25 nm, grain boundary deformation mechanisms are believed to dominate leading to a reduction in strength (termed inverse Hall-Petch) [1].

In applied materials, the Hall-Petch relation can be used to strengthen materials through control of grain size. Alloying is another common method of adding strength or ductility to a metal. Alloy strengthening can result through the formation of a solid solution or through precipitates that act as barriers to dislocation motion. In the case of the formation of solid solution (particularly in hexagonal crystals), this can also reduce the anisotropy between slip systems, increasing the number of available slip systems and leading to an increase in ductility.

1.2 Small-scale experiments and size effects in metals

Development in small-scale mechanical testing has revealed new insights into the physical mechanisms of crystalline deformation at sub-micron length scales. Extension of nano-indentation has led to techniques for nano-scale compression, tension, and bending testing. One of the more well-known conclusions from micro- and nano-scale mechanical testing on single crystalline metals has been the relation between the extrinsic sample size and flow stress. This single crystal size effect can be described by a power-law, $\sigma \propto D^{-n}$, where σ is the flow stress, D is a characteristic sample dimension, often the diameter for cylindrical samples, and n is an experimentally fit value [1,2]. The stress-strain signature of sub-micron crystals is characterized by intermittent strain bursts. These discrete events correspond to the activation of dislocation sources and the resulting avalanche of dislocations. These dislocations travel through the pillar and annihilate at the free surface, leaving a surface ledge corresponding to the Burgers vector displacement of the dislocation.

The mechanism of dislocation activity in sub-micron single crystals is source-driven [3–5]. In the free-surface dominated structure, mobile dislocations quickly escape out of the pillar requiring the activation of sources to accommodate further plastic deformation. For pillar diameters down to around 200nm, these sources are truncated Frank-Read sources that extend between an internal pinning point and the free surface. For smaller pillar diameters, the free surface can act as a source via dislocation nucleation from the free surface.

The dominance of the free surface in sub-micron metals can be challenged by the presence of an internal microstructure or a passivation layer covering the free surface. As an example, Pt nanopillars with a nano-crystalline microstructure show strength that decreases with pillar diameter [6]. This demonstrates the importance in understanding how microstructural interfaces effect the deformation of crystalline metals at the nano-scale.

1.3 Objectives and outline

This thesis will address the effects of microstructural interfaces on the mechanical behavior of sub-micron crystalline metals. Most studies discussed above observed deformation through dislocation-mediated plasticity and fewer studies has been performed to investigate the conditions necessary to observe grain boundary-mediated deformation mechanisms. These studies also tend to consider simple microstructures, most often single crystalline, cubic metals. Similar compression experiments on more complicated microstructures will lend themselves well to applications in conventional structural materials where complex microstructures are an unavoidable consequence of the fabrication process. We also hope that these investigations will contribute development of a measure of control in the mechanical properties of these boundary-containing materials towards the fabrication of novel materials.

Chapter 2 will summarize work done on Cu nanopillars with a conformal hard coating and introduces an analytic model that describes the emergence of the Bauschinger effect in unloading/loading cycles. Chapter 3 explores the deformation of Al nanopillars that contain a single grain boundary aligned along the pillar axis. Grain boundaries investigated include high-symmetry boundaries with coincident site lattice numbers of Σ3 and Σ5. Molecular dynamics simulations explore the atomic mechanisms occurring at the grain boundary and the interactions between dislocations and the grain boundary. Chapter 4 investigates grain boundary sliding dominated deformation through compression of Al nanopillars containing a single random grain boundary acutely tilted from the pillar axis. Molecular dynamics simulations on the shearing of planar grain boundaries reveals the atomic mechanisms that accommodate sliding. Chapter 5 reports the effect of alloying on Mg through compression of AZ31 nanopillars. We investigate the presence of solid solution and precipitate strengthening and crystal anisotropy. We also analyze the effect of crystal orientation on the dominant slip systems and the effect of crystal anisotropy on the size effect.

2. Effects of a Hard Surface Coating on Strength and Deformation of Single Crystalline Copper

2.1 Introduction

Manipulation of the mechanical properties of a single-crystalline metal through control of its extrinsic size has revealed much about the physics of crystalline deformation at micron and sub-micron length scales. It has been observed in mechanical testing of cylindrical, metallic single crystals that the flow stress will increase with decreasing sample diameter [1,2,7–10]. This trend is well described by a power law relation $\sigma_s \propto D^{-n}$, where σ_s is the material flow stress, *D* is the sample diameter, and *n* is an experimentally-fit strengthening exponent [3,11]. In contrast to bulk samples where forest-hardening typically drives strengthening [12], the physical mechanisms of plastic behavior at the sub-micron length scale is dislocation nucleation driven [4,5,9,13–15]. For the free-surface dominated sample, initial mobile dislocations will easily escape, requiring the activation of dislocation sources to accommodate further plasticity. The statistical models developed to describe source activation accord well with the above power law where activation strength is determined by the length of the source [3,13], a dimension limited by the presence of the free surface. As the stress required to activate a source approaches the heterogeneous nucleation stress, the free surface of the sample can also act and even dominate as a primary dislocation source [5,15].

The above emphasizes the importance of the free surface in sub-micron plasticity and suggests an opportunity of manipulation of the free surface as a means to control the mechanical behavior at the sub-micron length-scale. Passivation of the free surface and prevention of dislocation escape should result in a transition in the dominate mechanisms of plasticity. Previous studies on the effects of passivation on the mechanical properties of nano-scale metallic materials has focused on thin film geometries [16–18]. Bulge testing revealed increases in strength above unpassivated films and a

Bauschinger effect in unsupported Cu films with thicknesses between 300 nm to 1 µm coated with 80 nm thick Si_3N_4/TaN passivation layers. Some experiments on cylindrical geometries with a coating have also observed elevated flow stresses [19,20]. Post-deformation transmission electron microscope (TEM) images of single crystalline Al pillars with a W-Ga alloy coating revealed a build-up in dislocation density which the authors suggested led to the observed increased strength and post-yield hardening [19]. Both groups also noted an absence of bursts seen in previous single-crystalline compression experiments. The groups observed smooth, continuous stress-strain signatures. Loading was monotonic, so the presence of a Bauschinger effect could not be concluded.

Here we explore the role of a stiff conformal passivation layer on the mechanical deformation of single-crystalline Cu nanopillars. Nanopillars were coated with a 5-25 nm thick Al2O2/TiO2 layer deposited by atomic layer deposition. We performed uniaxial compression tests and explore the presence of the Bauschinger effect through several loading/unloading cycles. We explain the emergence of the Bauschinger effect by developing a dislocation theory-based analytical model. This work was originally published in *Acta Materialia* [21]. Experimental work was performed by Andrew T. Jennings and Cameron Gross.

2.2 Results of compression of conformally coated nanopillars

Cu nanopillars with initial diameters between 75 and 1000 nm were fabricated using template electroplating [22]. Atomic layer deposition (ALD) was used to conformally coat the nanopillars with 5-25 nm thick conformal layer of Al_2O_2/TiO_2. A scanning electron microscope (SEM) image of a representative coated nanopillar is shown in Figure 2.1a. Uniform compression tests were performed in an Agilent G200 nanoindenter using a 7 µm diamond flat punch. Compression was performed in displacement-controlled mode at a nominal strain rate of 10^{-3} s^{-1}. Unloading segments were performed at increments of 2% strain throughout the test to investigate the presence of the Bauschinger effect.

Figure 2.1b shows the stress-strain data for a representative conformally-coated nanopillar. The inset provides a higher magnification of the initial 4% of deformation. Hysteresis loops can clearly be seen during unloading/loading cycles while overall deformation up to failure remains nearly elastic with small strain bursts present, and ultimately followed by a significantly larger burst. Post-deformation SEM images (an example of which is given in Figure 2.1c) reveal that this large burst coincides with cracking and subsequent delamination of the hard coating.

In order to investigate the effect of the hard coating in preventing dislocation escape through the free surface, we performed post-deformation TEM analysis. Figure 2.2 shows a bright-field TEM micrograph of a representative nanopillar where the coating can be seen to have fractured off of the surface in some areas. Imaging contrast show dense networks of dislocations that have built up in the interior of the pillar. Streaking of spots seen in the inset diffraction pattern confirms the presence of significant lattice deformation. The observance of a dense dislocation density is in contrast to previous findings on sub-micron pillars that are generally characterized by a decrease in mobile dislocation density upon deformation and lack such dislocation substructures [22]. This suggests that the presence of the Al_2O_2/TiO_2 coating is acting to prevent dislocation escape, causing dislocation pile-ups and the subsequent development of dislocation networks.

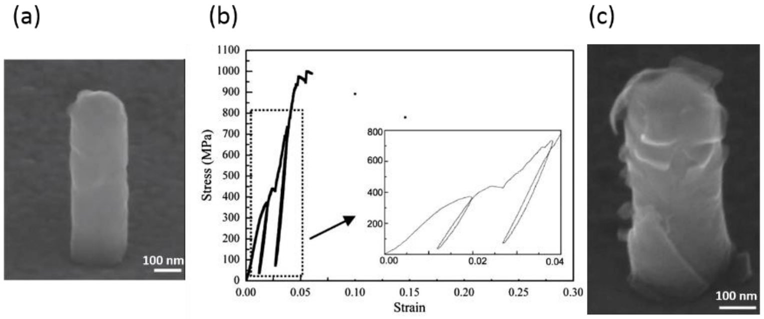

Figure 2.1: (a) Pre-deformation scanning electron microscopy image of a conformally coated Cu nanopillar. (b) Compressive stress-strain data from coated Cu nanopillars. Inset shows high magnification of loading/reloading segments, revealing hysteresis loops. (c) Post-deformation SEM image of coated Cu nanopillar given in (a). Failure corresponds to delamination of the hard coating.

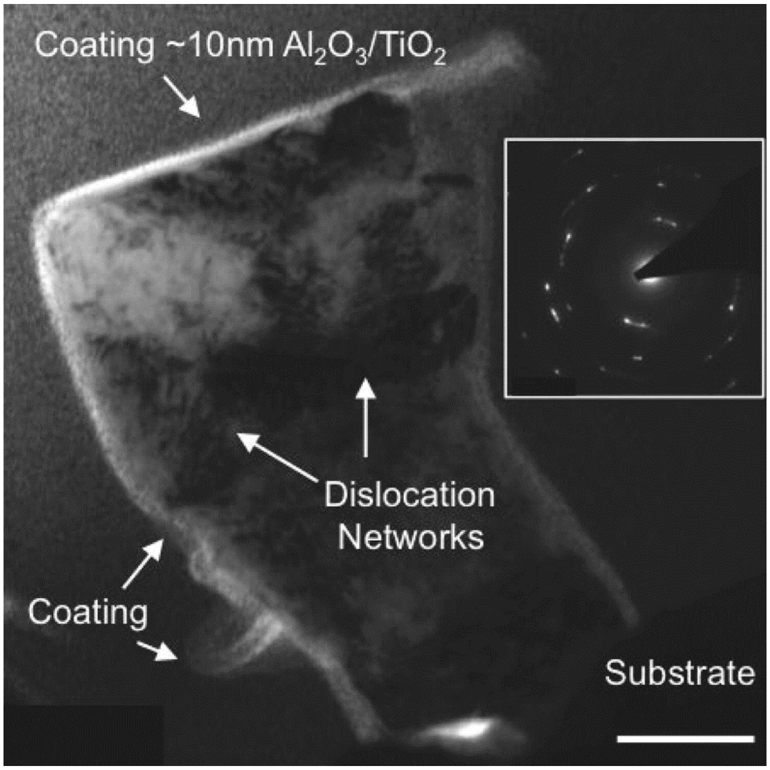

Figure 2.2: Post-deformation TEM micrograph of coating Cu nanopillar. Dense dislocation networks are observed within the pillar as pile-ups against the hard coating. The inset diffraction pattern shows streaking and is indicative of significant crystal deformation.

2.3 Analytic model for Bauschinger effect

In order to investigate the role of the coating as a source of hysteresis deeper within the pillar we developed a simple one-dimensional analytical model based on dislocation theory that predicts the emergence of hysteresis from dislocations piling up against the hard coating. Recent 3-D DD models on coated nanopillars considered the cases of (1) an impenetrable coating and (2) dislocations capable of breaking through the coating [23] and [24]. However, samples in these simulations were loaded monotonically and thus did not explore the loading–unloading hysteresis. Similar 2-D simulations of thin films with an impenetrable coating showed smooth hardening and a Bauschinger effect accompanied by hysteresis loops [25] and [16]. Each of these studies incorporates varying aspects of the broad complexity of this problem. As an alternative approach we considered an analytical model of the slip plane in isolation and employ classical dislocation theory to investigate compression of a coated nanopillar. In contrast to dislocation dynamics-based models, this relies on solving the quasi-static dislocation equilibrium configurations which do not rely on specification of mobility laws. In trade, this serves as an approximate problem in the hope of offering a physical interpretation of the Bauschinger effect. Hence, the aim of this model is not to act as an exact numerical comparison, but rather as a physically founded qualitative complement to the experimental results.

Starting with a cylindrical pillar, we isolated a resolved slip plane and considered it initially containing only a dislocation source offset from the center with a given strength τ_{source}. When activated, i.e., when the applied stress exceeds this strength, the source emits a dislocation loop, and has no short-range interaction with the dislocations it emits throughout the simulation. Viewed along a cross-section of the plane the resulting loop is seen as two oppositely oriented segments on either end of the slip plane, as shown in Figure 2.3a. As this slip plane is isolated we do not consider interactions with other slip planes or 3-D processes such as cross-slip. At the boundary of the domain is the coating with given strengths $\tau_{coating}$ and $\tau'_{coating}$ on either side, whose actual values may depend on elastic modulus or lattice mismatch, coating thickness, and orientation of the dislocation and interface [26]. Strengthening of these collective interactions represents the Koehler barrier strength that sets a threshold stress at which dislocations are allowed to pass through the coating [27]. Here we have taken $\tau_{coating} = \frac{4}{3}\tau'_{coating} = 4\tau_{source}$, values comparable with those used in previous coated pillar simulations [23]. The difference in coating strength arises from the variation seen in coating thickness and possible variations in its bonding strength that naturally arise during ALD deposition on a non-atomically smooth pillar surface. Figure 2.3a shows a geometrical diagram of the described set-up.

We take Cu as the representative materials and use it for all material properties. Beginning with the single-source in a dislocation-free plane, we incrementally apply a shear stress at a rate $\Delta\tau =$

$\pm 0.01\tau_{source}$. When the force concentrated at the source reaches $F = \tau_{source} b$, a loop is emitted and two oppositely oriented point segments are introduced into the slip plane at a distance $\delta x = 0.2L$ on either side of the source, where *L* is the length of the slip plane. The equilibrium positions of these dislocations are then determined through balance of the Peach-Kohler forces from long-range dislocation interactions and image forces caused by the hard coating. As an approximation, we truncate the image forces to the first image field. The Peach-Kohler force on the *i*th dislocation in a system of *N* dislocations is given by:

$$F^{i} = \tau_{applied} b - \frac{\mu b^{2}}{2\pi} \sum_{\substack{n=1 \\ n \neq i}}^{2N} \frac{sign(n,i)}{x_{n} - x_{i}} \qquad \text{Eq. (2.1)}$$

where we have treated the dislocations as screw-type, and where *b* is the Burgers vector and $sign(n, i)$ is read as the direction of the force on the *i*th dislocation by the *n*th dislocation. The summation is performed over both the real and image dislocations for *2N* total dislocations. Following the calculation of the equilibrium position of the dislocations, the force on the two dislocations closest to the coating is calculated to check if either exceeds their respective coating strength. This condition is:

$$\tau_{applied} - \frac{\mu b}{2\pi} \sum_{n=2}^{N} \frac{1}{x_{n} - x_{1}} \geq \tau_{coating} \qquad \text{Eq. (2.2)}$$

If this condition is met, this dislocation escapes through the coating and the equilibrium positions of the remaining dislocations are recalculated. If the condition is not met, then the applied stress is incremented until the sum of the applied stress and the back-stresses are larger than the source strength:

$$\tau_{applied} - \frac{\mu b}{2\pi} \sum_{n=0}^{N} \frac{1}{x_{n}} \geq \tau_{source} \qquad \text{Eq. (2.3)}$$

This process is iterated through loading/unloading and at each stress, the total strain is calculated by the elastic strain given by Hooke's law and the plastic strain that is proportional to the distance swept out by the dislocations:

$$d\varepsilon_{plastic} = \frac{1}{2}\frac{b}{V}dA \qquad \text{Eq. (2.4)}$$

For *y* indicating the direction normal to the plane and z directed out of Figure 2.3a, we can take a representative volume, $V = L_x L_y L_z = 3L^2 L_z$, with L_z being arbitrary for the 1-dimensional problem. With $dA = L_z dx$, the expression for plastic strain simplifies to:

$$d\varepsilon_{plastic} = \frac{1}{6}\frac{b}{L^2}dx \qquad \text{Eq. (2.5)}$$

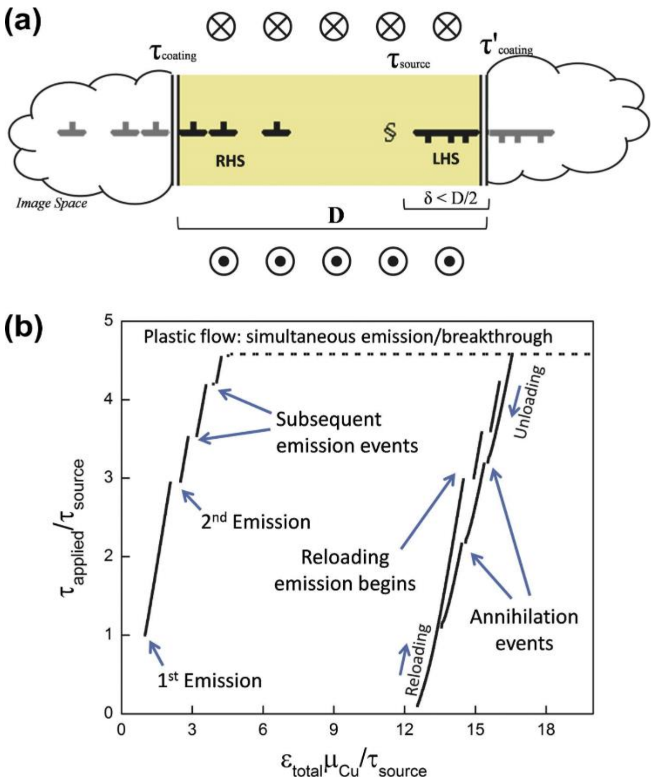

Figure 2.3: (a) A 2-D schematic showing pillar geometry for the analytical model. The yellow region corresponds to the pillar cross-section, and cloud-like regions on both sides represent the dislocation image space. Dislocations are treated as screw-type and shown as ⊥ or T depending on dislocation orientation. The section sign (§) corresponds to the dislocation source, and gray dislocations in the image space represent image dislocations. For screw-type dislocations the applied shear vectors

directed into and out of the page are shown above and below the plane. (b) Shear stress normalized by the source strength vs. the dimensionless strain parameter generated by the analytical model with material properties representative of Cu, $\mu_{Cu} = 48$ GPa and b = 0.256 nm.

Figure 2.3b shows the stress–strain curve resulting from the model, where the strain is a summation across 10 identical slip planes. Starting with emission of the first loop, the loading curve is marked by discrete events, each corresponding to source activation. This continues as the traveling dislocations pile up against the coating. Eventually continuous plastic flow (with no hardening) begins, where the applied stress is sufficiently high that both source emission and coating penetration occur simultaneously. Plastic deformation continues until unloading, when the dislocations move back towards the center of the domain and annihilate when two oppositely oriented dislocations are in proximity of each other. The applied stress is then increased, and a clear deviation of the reloading curve from the unloading curve is apparent. This hysteresis loop is only seen when a coating strength is applied at the boundary. In exploring the virtues and limitations of this model we see that, as expected, the model shows no difference in stress–strain curves between the unloading vs. reloading directions for the case of free surfaces, which suggests that the Bauschinger effect is caused entirely by the presence of the coating. While it is a necessary condition for the Bauschinger effect, it is not sufficient. Not just dislocation storage, but asymmetric dislocation storage is sufficient to observe hysteresis. In simulations where the dislocation source was placed directly in the center of the slip plane and the coating had equal strengths on both sides, no hysteresis was observed. In this 1D model, asymmetric storage can be achieved through differences in the coating strength. When break-through is achieved, dislocations on one side will escape leaving their corresponding segment on the opposite side of the plane.

In contrast to earlier DD simulations on uncoated sub-micron copper-like pillars that exhibited a Bauschinger effect [28], this model treats each dislocation source as independent, i.e., the dislocations produced from one source do not interact with dislocations from a different source. As a result, during either the loading or unloading phase of the hysteresis loop in Figure 2.3c the deviation of the stress–

strain curve from linear elasticity is a result of the emission and movement of dislocations (plasticity gained) or relaxation and annihilation of dislocations (plasticity recovered). Considering an increase in coating strength, more dislocations will be stored within the coating and thus greater deviation will occur. We would then expect to see an increase in hysteresis with an increase in coating strength. These modeling results are encouraging in that they appear to capture the behavior seen experimentally in a model that is not computationally expensive and can be interpreted through classical dislocation theory.

2.4 Summary

In conclusion, uniaxial compression experiments on 75-1000 nm diameter electroplated single crystalline Cu nanopillars coated with a conformal 5-25 nm layer of Al_2O_3/TiO_2 displayed higher strengths compared to as-fabricated counterparts. Hysteretic loops were observed during unloading/reloading cycles whose magnitude increased with pre-strain. We have developed an analytical model based on classic dislocation theory to investigate the emergence of the Bauschinger effect in pillars with a hard coating. Hysteresis loops are observed in the data generated by the analytic model and seen to be a result of an asymmetric build-up of dislocation density with strain.

3. Strength and Deformation of Nano-scale Aluminum Containing a Single, Vertically-Aligned Grain Boundary

3.1 Introduction

The development of nano-scale mechanical testing has led to insights in the plasticity of small-scale crystalline metals of various microstructures including: nano-laminate [29,30], nano-twin [31,32], single crystalline, and nanocrystalline microstructures [6,33]. The small sample volume lends itself well to investigating the effect of isolated microstructural features on the deformation dominant mechanisms. In contrast to single crystalline metals, nano-crystalline nanopillars of similar size and material show a weakening, rather than strengthening with pillar diameter [6]. This reversal of mechanical behavior highlights the importance that the microstructure has in determining mechanical properties at these length scales.

Previous studies on cylindrical compression samples containing a single grain boundary have focused on random grain boundary types oriented vertically within the cylinder [34–36]. Ngan et al. investigated compressive response of 6 Al µm-diameter micro-pillars, each containing a general high-angle grain boundary [34]. Transmission electron microscopy analysis revealed that the grain boundary was not vertically-aligned as presumed, but extended at an angle from the top of the pillar to somewhere along its mid-section. These authors noted substantial strain hardening in the compressive stress-strain response of the Al bi-crystals, in contrast to single crystalline Al samples of equivalent diameters. They also observed significant dislocation pileups near the grain boundary after the deformation, which suggests that the grain boundary was acting as an obstacle to dislocation motion.

Kheradmand and Vehoff investigated compression of Ni pillars, each containing a vertically-aligned high-angle boundary, with diameters ranging from 1–7 µm and fabricated by focused ion beam (FIB) [36].

These authors observed a 76–97% increase in yield stress compared with single crystalline specimens only in the samples with diameters of 1.4–2 µm. Orientation Imaging Microscopy indicated that the dislocation density in the vicinity of the grain boundary increased, which suggests that the grain boundary acted as an obstacle to dislocation motion. The authors also observed slip transmission across the grain boundary and a minimum density on slip bands where transmission occurred, which was explained by the local rotation in the course of compression, which rendered the grain boundary no longer an obstacle to dislocation motion.

Kunz et al. performed uniaxial compression experiments on a range of bicrystalline Al pillars, with diameters spanning from 400 nm to 2 µm each containing a high-angle boundary oriented parallel to the pillar and to the compression axis [35]. No significant hardening or distinctions from the single crystalline samples of equivalent diameters were observed in the stress strain response of these samples. TEM investigations displayed a low dislocation density near the grain boundary, more similar to the density near the free surface than within the body of the pillar. They concluded that this particular grain boundary likely absorbed the gliding dislocations and was acting as a sink for these defects.

This overview of the deformation of metallic micro-bicrystals demonstrates that for an isolated grain boundary, both the orientation of the boundary with respect to the loading direction and the pillar size can result in contrasting stress-strain response and microstructure evolution. Along with the five degrees of freedom that specify the crystal orientation of the component grains and boundary orientation, the atomic degrees of freedom play a role in the dislocation-grain boundary interaction [37]. A lack of atomic information of the grain boundary configuration makes it difficult to compare boundary behavior between samples.

Here we present the effect of a single, vertically-oriented coincident site lattice (CSL) grain boundary on the mechanical deformation of Al nanopillars. We investigate both Σ3 and Σ5 grain boundaries, grain boundaries that contain a high number of well-known, coherent grain boundary sites. We also perform molecular dynamics simulations on nanowire containing either a single high-angle or CSL grain boundaries of known orientation to elucidate the atomic mechanisms that drive deformation. Portions of this work were first published in *Modelling and Simulation in Materials Science and Engineering* [38]. Molecular dynamics simulations were performed by Garritt J. Tucker and Christopher R. Weinberger (both now at Drexel University) at Sandia National Laboratories.

3.2 Grain boundary characterization and mechanical testing

3.2.1 EBSD Characterization

Compression samples were fabricated from a bulk sample of polycrystalline Al. The surface had been previously smoothed by electropolishing and the grain size and texture had been analyzed by electron backscatter diffraction. Using the grain orientation information and commercial Channel 5 analysis software (HKL Research Inc.) we identified several highly symmetric grain boundary orientations. These crystallites are related by one of the characteristic coincident site lattice rotations. In this bulk sample, we have identified grain boundaries exhibiting a $\Sigma3$ and $\Sigma5$ CSL-type lattice. Figure 3.1a shows the grain orientation map where the $\Sigma3$ and $\Sigma5$ boundaries are labeled and the individual orientations are given on the stereographic triangle in Figure 3.1b.

3.2.2 Sample fabrication and compression experiments

Compression samples are fabricated within a dual-beam SEM (FEI) using the top-down focused ion beam methodology [8]. A series of annular patterns with successively decreasing diameter were used to remove material resulting in a cylindrical geometry. Ion milling was performed at 30 keV with decreasing current from 3 to 0.05 nA. A representative compression sample is shown in Figure 3.1c. Compression samples containing a GB were fabricated by applying this methodology along the target GB. Single crystalline compression samples were also fabricated from within the bulk of each component crystallite.

Uniaxial compression experiments were performed in a nanoindenter (Triboscope, Hysitron Inc.) using a diamond flat punch tip with a diameter of 8 µm. Tests were performed under displacement-rate control, at a nominal strain rate of 10^{-3} s^{-1}. The displacement was monitored continuously at a frequency of 78 kHz via a feedback loop through the Hysitron *performec* control module. Engineering stress and strain were calculated by dividing the force and displacement by the initial cross-sectional area and pillar height, respectively. For comparison to previous studies, applied stress was resolved onto the slip system with the greatest Schmid factor among both component grains and recorded at 7.5% strain. 19 nanopillars were tested along the Σ3 boundary and 10 nanopillars were tested along the Σ5 boundary. Of these, 13 Σ3 nanopillars and 9 Σ5 nanopillars showed no evidence of bending or misalignment of the indenter tip and were considered reliable tests.

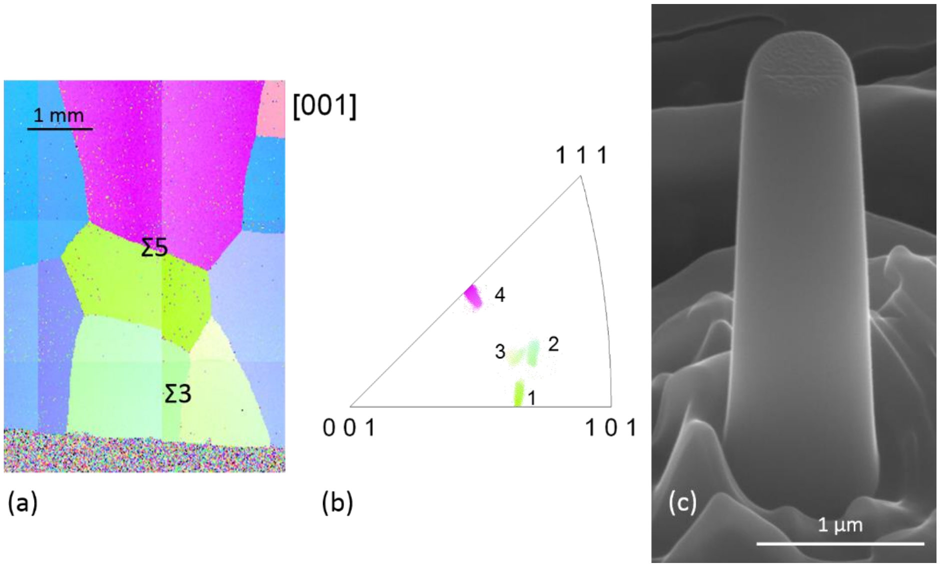

Figure 3.1: (a) Crystal orientation map of grains used to fabricate compression samples. Grain boundaries of Σ3 and Σ5 are labeled. (b) Stereographic triangle showing the crystal orientations of each constituent grain. (c) SEM image of an example bicrystalline nanopillar.

3.2.3 Coincident site lattice

The coincident site lattice refers to the grain boundary lattice that results from points of coincidence between the two crystalline lattices that compromise the grain boundary. The Σ-number is equal to the inverse of the ratio of coincident sites to total sites. For example, Σ3 implies that 1 out of every 3 sites at the grain boundary is a coincident site. Grain boundaries with low Σ-numbers therefore have a large number of coincident points and relatively low energy in contrast to previous studies that have focused nearly exclusively on high-angle, high-energy grain boundaries. The high number of coincident points in low Σ-number boundaries also lends itself well to molecular dynamics studies, where the atomic boundary structure can be easily modeled.

The Σ3 boundary is a special example of a highly-coincident boundary that is more commonly referred to as a twin boundary. Previous reports on twin-dislocation interactions have investigated Cu nanopillars containing twin boundaries spaced between 0.6-4.3 nm apart [31]. The authors observed that twin boundaries can serve as sources of dislocations and can interact with impinging dislocations, forming mobile Shockley partials capable of slipping on twin boundaries. Alternatively, transfer across Σ3 boundaries has been observed in Cu micropillars [39,40]. Suggested explanations include coherent slip systems that allow for slip across the boundary [39] and transfer via cross-slip of screw dislocations [40].

3.2.4 Nano-scale compression experiments

Figures 3.2a and 3.2c show post-deformation SEM images of a Σ3 and Σ5 pillar with their associated stress-strain data. Stress-strain data in both types of grain boundaries is characterized by intermittent bursts also frequently observed in similar compression tests on single crystalline metals [1,41]. These bursts are attributed to dislocation avalanches released from their pinning points that get activated as dislocation sources under applied stress [42,43]. These dislocations then freely travel across their slip plane and annihilate at the free surface. It must be noted that calculation of stress can prove difficult due to the discrete and stochastic changes in pillar geometry after yielding. Here we use the initial pillar configuration as the reference geometry and, with respect to this initial geometry, no significant strain hardening is observed in either Σ3 or Σ5 compression samples, suggesting the absence of barriers to dislocation motion.

Figure 3.3 shows the resolved stress at 7.5% strain of CSL-containing compression samples plotted against sample diameter. Also shown are resolved stresses at 7.5% of high-angle Al bicrystalline nanopillars from Kunz, et al. [35]. Flow stresses for all samples increase with decreasing pillar diameter, following the single crystalline trend [1,2]. The power law exponent for the size effect is identical in both Σ3 and Σ5 nanopillars at 0.91 and is much greater than the exponent of high-angle GB Al bicrystalline nanopillars at 0.58 [35]. Strengths match well with Al bicrystals from Kunz [35].

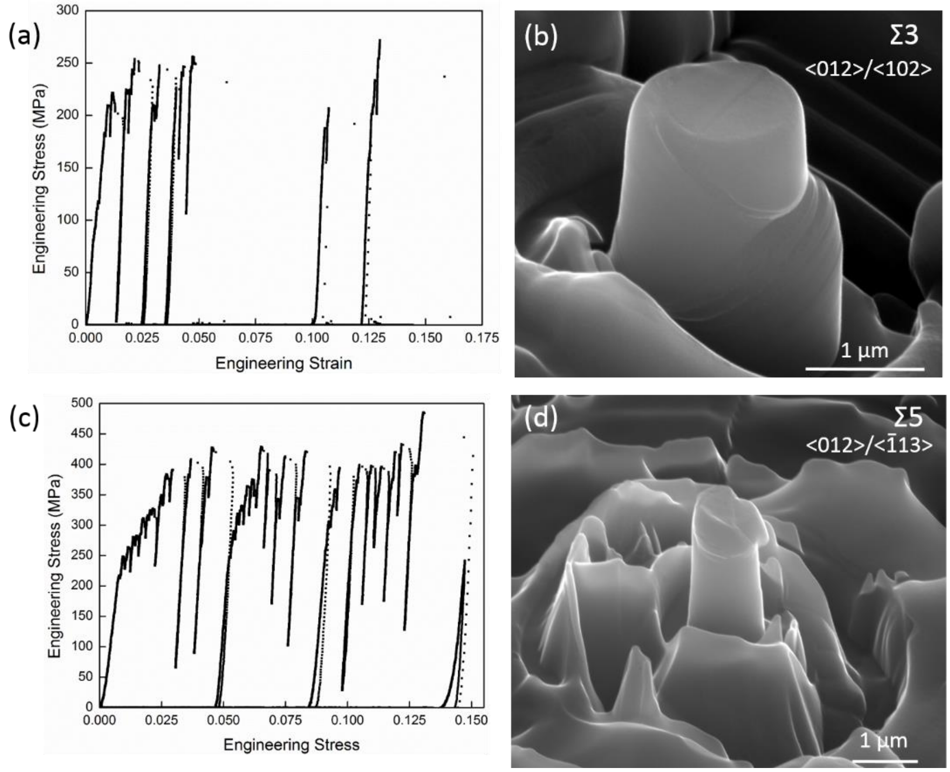

Figure 3.2: (a) Engineering stress-strain data for an example Σ3 bicrystalline compression sample. (b) Post-deformation SEM image of Σ3 bicrystal. Shear offsets are seen to pass through the entirety of the pillar, including the grain boundary. (c) Engineering stress-strain data for an example Σ5 bicrystalline compression sample. (d) Post-deformation SEM of Σ5 bicrystal.

It is not readily apparent whether the difference in power law exponent is due to the presence of the CSL boundary or differences in initial dislocation density. A lower initial dislocation density in the CSL bicrystals would result in an increased sensitivity to sample size. The stress-strain signatures of these samples do not vary significantly from single crystalline Al and post-deformation SEM images show slip planes traversing the boundary. These observations demonstrate that Σ3 and Σ5 boundaries do not act as an obstacle to dislocation motion. Similar to reports in bicrystalline Cu micropillars [39], the presence of coherent shear offsets that extend the entirety of the pillar diameter suggest the possibility of matching slip systems that allow dislocations to pass through the boundary. Further analysis of the crystallographic orientation information obtained from EBSD will be required to explore the possibility of coherent slip systems.

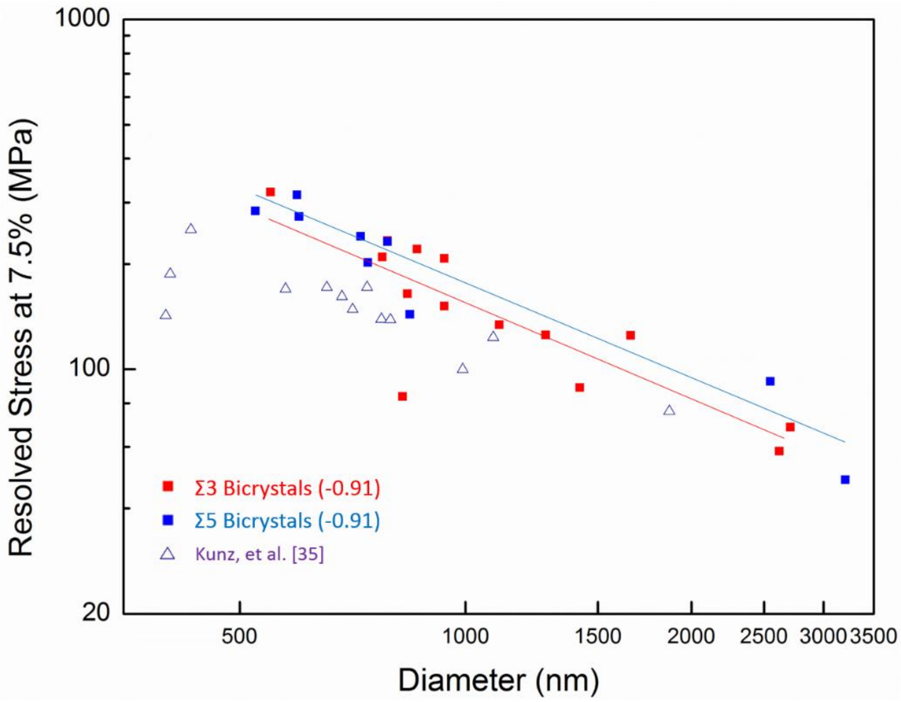

Figure 3.3: Resolved shear stress at 7.5% strain against pillar diameter. Included is stress data from Σ3 and Σ5 compression samples and data from Kunz, et al. [35].

3.3 Molecular dynamics simulations

3.3.1 Methodology

Bicrystalline nanowires were constructed by generating a 3D periodic bicrystalline configuration consisting of two crystalline lattices separated by a planar grain boundary. Employing an Al embedded atom method (EAM) potential [44] and molecular statics, the total energy of the bicrystal was minimized using a conjugate gradient scheme to create the initial grain boundary configuration. Prior to energy minimization, numerous in-plane rigid body translations of one lattice relative to the other were undertaken to better approximate the lowest energy configuration. From these bicrystals, a 30 nm diameter cylinder was cut such that the grain boundary plane aligned parallel with the long axis of the cylinder and was centered within the nanowire. Periodicity was maintained along the wire axis and free surfaces were applied in the two transverse directions. Simulations were performed using the LAMMPS molecular dynamics software package [45] and visualizations were generated using AtomEye [46] and OVITO [47]. Simulations were performed at 300K and time integration of atomic position and velocity was performed by sampling the isothermal-isobaric ensemble using a Nose-Hoover thermostat. We studied three random high-angle grain boundaries and a series of symmetric tilt boundaries. Figures 3.4a and 3.4b show side and axial views of the generated high-angle bicrystal. Atoms in Figure 3.4b are colored by their centrosymmetric value [48] and undisturbed atoms have been removed for clarity. Figure 3.4c provides a stereographic triangle with the orientations of the three high-angle bicrystal systems studied.

Compression was induced by decreasing the periodic dimension of the simulation box at a nominal strain rate of 10^8 s^{-1} up to a final 20% engineering strain. Stress was calculated every 5 ps following the atomic virial stress definition:

$$\sigma_{ij} = \frac{1}{N\Omega}\sum_{\alpha}^{N}\sum_{\beta\neq\alpha}^{N^{\alpha}} f_i^{\alpha\beta}\, r_j^{\alpha\beta} \qquad \text{Eq. (3.1)}$$

where Ω is defined as the atomic volume, N represents the total number of atoms in the system, N^{α} represents the number of neighboring atoms for each atom α, $f_i^{\alpha\beta}$ defines the interatomic force vector between each atom α and its neighbor β in the *i* direction, and $r_j^{\alpha\beta}$ is the interatomic distance of atoms α and β in the *j* direction. The common neighbor analysis method was performed along with stress to compute the local crystal structure of each atom.

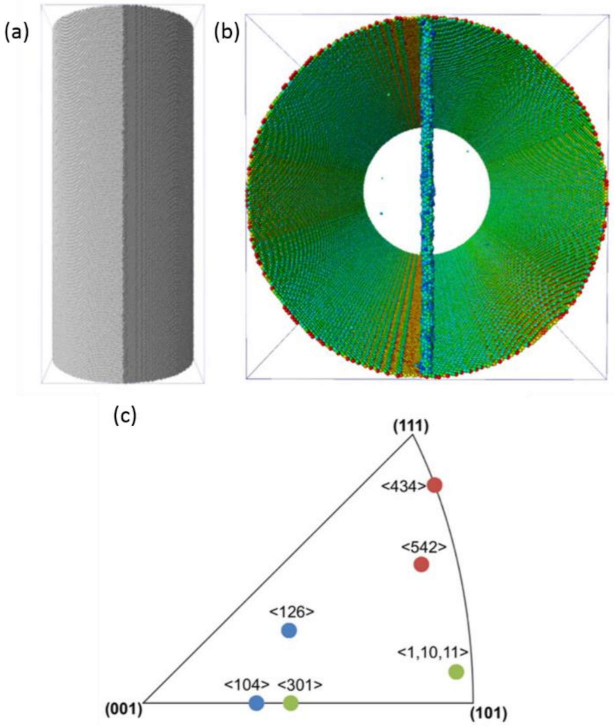

Figure 3.4: (a) Side view of bicrystalline nanowire generated for MD simulations. (b) Axial view of bicrystalline nanowire. Atoms are colored based on their centrosymmetric parameter and inner lattice atoms have been removed for clarity. (c) Stereographic triangle showing the crystal orientations of the three simulated high-angle bicrystal systems.

3.3.2 Results

3.3.2.1 *High-angle grain boundaries*

Figure 3.5 shows the stress-strain data generated from compression simulations on 3 different bicrystalline nanowires. All 3 nanowires reach approximately the same peak stress, but display differing plastic behavior. The post-elastic behavior varies from smooth deformation to stick-slip deformation.

Figure 3.6a shows an axial cross section of a nanowire at 5% strain. Atoms are colored by their crystal structure as determined from common neighbor analysis (CNA) [49,50]. The initial dislocation nucleation event shown in Figure 3.6a occurs within the high-symmetry crystallite and occurs at the intersection of the interface and surface. After initial nucleation, the dislocation travels through the crystal, depositing Burgers vector content into the boundary, which is behavior consistent with the GB acting as a sink. Unimpeded dislocation glide results in dislocation starvation, where additional dislocations must be nucleated to accommodate the applied strain. This mechanism of additional nucleation leads to the stick-slip behavior seen in the stress-strain <434>/<542> bicrystal. If migrating dislocations are instead momentarily trapped by lattice defects or there is the presence of a mechanism that more easily nucleates new dislocations, the plastic behavior appears smooth, like that seen in the <1,10,11>/<301> bicrystal. In these nanowires, twin boundaries are observed that serve as preferred nucleation planes and paths for dislocations and requires lower axial stress to nucleate new dislocations. This decreased nucleation stress and preferred slip path contributes to a smoother post-elastic stress-strain signature.

At high compressive strain, after several lattice dislocation interactions and absorption events, full dislocation loops are seen to nucleate from the GB into the lattice. Figure 3.6b shows the same cross-section as seen in Figure 3.6a at a high compressive strain, where dislocations loops can be seen nucleating from the GB on the {111} slip planes. In all three high-angle bicrystalline nanowires, there was no evidence supporting the GB acting as an obstacle to migrating dislocations. No dislocation pile-ups or pinned dislocations were observed near the GB for long periods of time. All lattice dislocations were either absorbed by the interface or exited through the free surface.

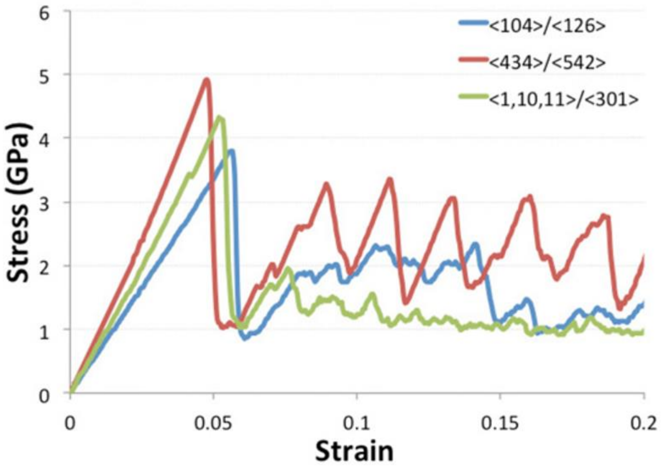

Figure 3.5: Compressive stress-strain data for all high-angle bicrystalline nanowires. Peak stress is similar between all bicrystals while plastic stress varies from stick-slip behavior to smooth deformation.

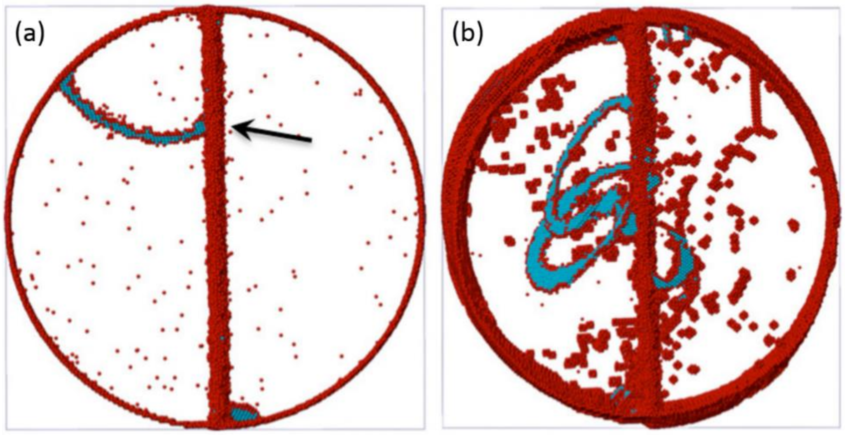

Figure 3.6: (a) Axial view of the initial nucleation event. Emission occurs at the intersection of the GB and the free surface. (b) Nucleation of full dislocation from the GB into both crystals is observed after significant deformation. All atoms are colored by their CNA value and FCC atoms are removed for clarity.

3.3.2.2 *Symmetric-tilt grain boundaries*

Figure 3.7a summarizes the stress-strain data generating from compression simulation on a bicrystalline nanowire containing a symmetric-tilt grain boundary. Boundaries studied include Σ129, Σ11, and Σ3. The interface has negligible effect on the stress of the initial nucleation event. The single-crystalline (i.e., 0° tilt) displays stick-slip plasticity due to dislocation exhaustion. All other symmetric-tilt bicrystalline nanowires display similar smooth plastic signatures. In each case, full dislocations are initially nucleated and then emitted from <100> surface facets. In both low and high-angle symmetric structures, the interface acts as a sink for incoming dislocations. Any impedance of the dislocation motion by the GB is temporary. Dislocation pile-ups were not observed during compression.

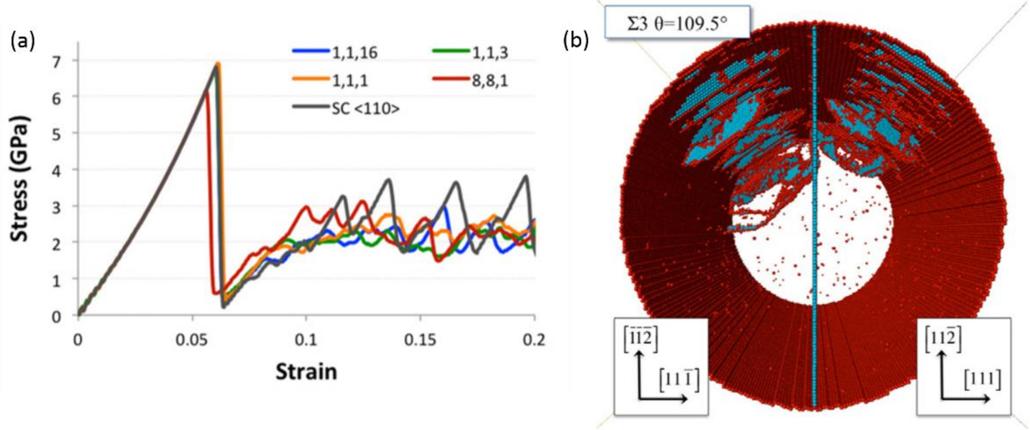

Figure 3.7: (a) Compressive stress-strain data for all symmetric-tilt bicrystalline systems. (b) Axial view of nucleation within Σ3 nanowire. Nucleation occurs from the free surface within both crystals.

Figure 3.7b shows the initial nucleation event in the Σ3 nanowire. In the case of the Σ3 nanowires, the boundary would absorb the incoming dislocation to create a GB or twin dislocation. Subsequently, emission of a full dislocation into the opposite lattice and back into the original lattice on the incoming {111} plane returns the Σ3 boundary to its low energy structure. This demonstrates an energetically-favorable mechanism in Σ3-containing nanowires that allows for transmission of dislocations across the grain boundary without significant deformation of the boundary, a conclusion consistent with the experimental observance of slip traces traversing the grain boundary.

While a single EAM potential was used in this study, it has been observed that the potential can affect the activation energy for diffusion in Al Σ5 boundaries [51]. In the high-angle grain boundaries, this could lead to differences in atomic migration along the grain boundary and thus distribution of Burgers vector content absorbed from migrating dislocations. In the symmetric-tilt grain boundaries, this could play a role in the mobility of grain boundary dislocations.

3.4 Summary

In summary, we performed compression experiments on Al bicrystalline nanopillars containing a single CSL grain boundary of either a Σ3 or Σ5 character. Stress-strain data was similar to single crystalline data and did not display any evidence of mechanisms that impeded dislocation motion. Post-deformation SEM images revealed slip traces that passed through Σ3 CSL grain boundaries. The CSL grain boundaries did not appear to have an impact on the size effect, displaying similar scaling to single crystalline samples. We also performed molecular dynamics simulations on bicrystalline nanowires containing a single random grain boundary and nanowire containing a symmetric-tilt grain boundary. Random grain boundaries were observed to initially act as a sink to dislocations and a source of dislocations with further straining. Symmetric-tilt grain boundaries did not act as boundaries to dislocation, but absorbed incoming dislocations and emitted dislocations into both component crystals. No dislocation pile-ups were observed in either random or symmetric-tilt grain boundaries. The grain boundaries do not act to impede dislocation motion and can function as dislocation sources or allow dislocation transmission, as seen in simulated Σ3 nanowires.

4. Room Temperature Grain Boundary Sliding in Nano-scale Aluminum

4.1 Introduction

Grain boundaries in crystals present an intriguing mystery in the materials sciences because of a paucity of reports on their atomic structure, morphology, and deformation properties. Multiple studies indicate that at high temperatures the grain boundaries slide past one another to carry plastic strain, while at room temperature deformation is dominated mainly by dislocation motion and their interactions with the grain boundaries. The limited number of experimental reports on the energetic and structural landscape of grain boundaries renders modeling of the general grain boundaries a particularly challenging task. Most of the existing literature is focused on well-defined, special boundaries such as symmetric tilt or pure twist boundaries [37,52–54].

The development and extensive use of the uniaxial micro- and nano-pillar uniaxial compression methodology has allowed for studies on metallic nanopillars with a variety of microstructures including: single crystalline, nano-twinned [31], nano-crystalline [6,33], bi-crystalline [34,35], and amorphous metallic glasses [55], each exhibiting unique mechanical behavior. A main finding from the uniaxial deformation experiments on single-crystalline metallic micro- and nano-sized samples is the emergence of a power law dependence of their flow stresses on sample dimensions [1,2]. This is in contrast to the classical theory, which dictates crystalline strength to be independent of sample size. The size effect in the nano-sized single crystals was attributed to the plasticity mechanism being dominated by dislocations nucleating either from single-arm sources [4,13,14] or from surface sources [5,15,56] rather than by dislocation multiplication, as in bulk [12]. In contrast to the single crystalline metals, the nano-crystalline nanopillars of similar size and material show a weakening, rather than strengthening, with pillar diameter. This reversal of mechanical behavior highlights the importance that the microstructure plays in determining mechanical properties at these length scales.

Reported experiments on bicrystalline micro- and nano-pillars have concentrated on random, high-angle or CSL-type grain boundaries that are oriented vertically or at an angle from the pillar axis [34–36]. Deformation in these pillars was accommodated by dislocation activity and no significant movement of the grain boundary was observed during compression. Interactions between dislocations and the grain boundary were seen to differ between grain boundaries and possibly dependent on the orientation of the boundary with respect to the loading direction and pillar size. This limited loading configuration results in no shear stress acting across the grain boundary and limits the available deformation mechanisms. The lack of investigation into the mechanical behavior of isolated grain boundaries under more varied loading configurations limits the current understanding of grain boundary deformation mechanisms because such axial loading results in no shear stresses acting along the grain boundary.

We conducted room-temperature uniaxial compression experiments on bi-crystalline Al nanopillars with diameters of 900 nm, each containing a single grain boundary, whose plane normal was inclined at an angle of approximately 24–28° from the loading direction. This orientation was intentionally chosen to subject the grain boundary to applied shear loading, in contrast to nearly all existing reports on the deformation of small-scale metallic bi-crystals. We observed the deformation to commence via a gradual sliding process along the grain boundary, where the top crystallite sheared off as a single piece with respect to the bottom one, with no evidence of any other significant plastic deformation. The stress-strain response contained an initial peak at a strain of 1%, which corresponded to the initiation of the shear offset, and a subsequent softening followed by a decrease and increase in stress between 79–112 MPa over 12% compressive strain. The data was continuous, showing no stochastic bursts. TEM analysis revealed no apparent dislocation debris at the grain boundary. We also performed molecular dynamics compression simulations on bicrystalline nanopillars containing a single tilted grain boundary at a tilt angle between 0° to 55° from the pillar axis and shearing simulations on a planar grain boundary. These simulations reveal a transition from dislocation-mediated plasticity to grain boundary-dominated deformation with increasing tilt angle. Shearing simulations show qualitatively similar stress-strain signatures and reveal a mechanism of atomic migration that facilitates grain boundary sliding.

4.2 Experimental

4.2.1 EBSD characterization and sample fabrication

Samples were prepared from a block of high purity aluminum poly-crystal that had been previously annealed under vacuum at 350 °C overnight, followed by electro-polishing. Pillars were carved using a subtractive etching methodology in the Focused Ion Beam (FEI Nova 600) [8]. Electron backscatter diffraction (EBSD) was used to characterize the location of the grain boundary and orientation of each grain. Figure 4.1a shows an orientation imaging microscopy (OIM) crystallographic map of the crystal face from which the samples were fabricated, with the specific boundary studied denoted by the dashed rectangle. In contrast to the typical top-down fabrication methodology of vertically-oriented pillars utilized by multiple research groups [5,8,42,57,58], here (once a suitable boundary was located) the sample stage was tilted within the chamber such that the surface normal was inclined at 35° relative to the ion beam column and the pillars were milled using an annular pattern. The inner diameter of the final annulus was 1 µm, resulting in a typical actual pillar diameter of ∼900 nm, with the final pillar height maintaining an aspect ratio (height/diameter) between 3:1 and 4:1. The inclination between the samples surface normal and the ion beam led to the non-orthogonal orientation of the pillar tops with respect to the pillar axis. The sample was then rotated by 180° within the chamber and inclined such that the ion column was perpendicular to the pillar axis. Utilizing a rectangular milling pattern, the inclined pillar top was flattened (Figures 4.1b and 4.1c). A SEM image of a representative sample with a tilted grain boundary is shown in Figure 4.1c, where the grain boundary can be seen extending from near the head of the pillar towards its base at the angle of 66° with respect to the horizontal.

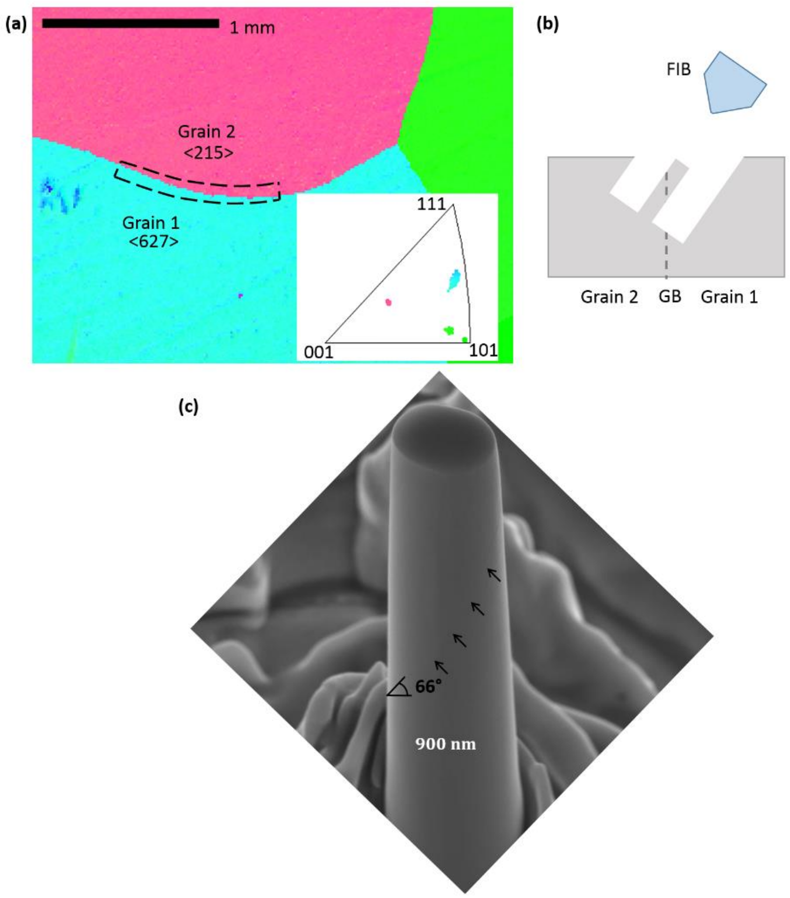

Figure 4.1: (a) Orientation Image Microscopy map generated by EBSD, which shows 3 grains in the top surface of the bulk Al crystal. The region along which the pillars were made is indicated by the bashed boundary. The inset shows the stereographic triangle with the grain orientations of <627> and <215>. (b) Schematic of the FIB milling process where the ion beam is tilted 35° from the sample surface normal. (c) A representative pillar (~900 nm diameter) containing a grain boundary inclined 66° above horizontal. The arrows below the boundary trace its path along the pillar surface.

Compression testing of all pillars was performed in a nanoindenter (Triboscope, Hysitron Inc.) using a diamond flat punch tip with a diameter of 8 µm. The tests were conducted under displacement rate control, at the nominal strain rate of 10^{-3} s^{-1} up to 15% total strain. The displacement was monitored continuously at a frequency of 78 kHz via a feedback loop through the Hysitron performec control module. True stress and true strain were calculated from the measured load and displacement data by following the methodology [8] and were corrected for the machine and the substrate compliances, as well as the thermal drift. Prior to compression, the bulk Al sample was mounted on a specially-made wedge sample holder that rotated the sample in order to orient the axis of each tilted pillar parallel to the indenter column. 7 nanopillars were constructed along the boundary although the orientation of the grain boundary within the nanopillar prior to compression could only be verified through SEM imagining within 2 of these samples.

Analysis of microstructure in the deformed samples was performed via transmission electron microscopy (FEI, Tecnai F30) at an accelerating voltage of 300 kV. Samples were lifted out from the parent crystal using a micromanipulator within the FIB (Omniprobe, Inc.) and attached to a TEM grid with ion-beam assisted, site-specific, Pt deposition. Once attached to the TEM grid, the samples were thinned using decreasing current down to 10 pA to a thickness of <100 nm to ensure electron transparency.

4.2.2 Compression experiment results

Figure 4.2b displays compressive stress-strain data for a representative 900 nm diameter sample. The plot shows that elastic loading led to a maximum axial stress of 156 MPa, after which the stress decreased abruptly to 100 MPa at the strain of 2.5%, slightly increased up to 112 MPa at 4.2% strain, and then gradually decreased to 79 MPa at 14% strain before rising to 100 MPa at the unloading strain of 16.2%. The data appears to contain some high-frequency oscillations after the local minima in stress at 2.5% strain and does not exhibit strain bursts typically seen in micron- and nano-scale pillar compression tests [41].

Figure 4.2c shows the post-deformation SEM image of this sample and reveals that virtually all plastic deformation was carried out by a single shear offset at a tilt angle of 66° from the horizontal. The created surface formed along the grain boundary (Figure 4.2c). Examining the sheared off regions revealed that the exposed surface had wavy features (Figure 4.2c), periodically spaced ∼50 nm apart, and some slip lines near the top of the pillar. Among all samples tested, this behavior could be verified in

3 nanopillars. Earlier work on uniaxial compressions of similarly fabricated bi-crystalline Al cylinders of equivalent diameters, which contained a high-angle grain boundary oriented along the compression direction, exhibited substantially different response, including post-elastic hardening, stochastic stress-strain signature, and significant crystallographic slip [35]. This highlights the influence of grain boundary orientation with respect to the loading direction on the deformation mechanism: the frictional sliding of the top grain occurred only in those bi-crystals, where the grain boundary experienced applied shear stress.

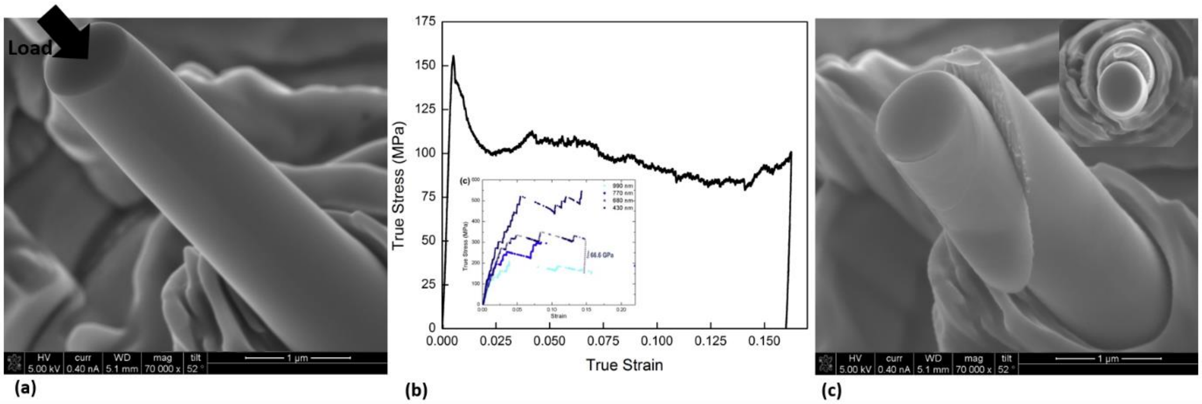

Figure 4.2: (a) SEM image of an as-fabricated pillar before uni-axial compression with the direction of applied load shown by the black arrow. (b) Stress-strain data of the same pillar collected during the compression experiment. Yield corresponds to the maximum peak stress at the strain of 0.5%, after which it rapidly softens, and plastic flow commences at a gradually decreasing stress to the final unloading strain of ~16%. The compressive stress-strain data of Kunz et al. [35] of bicrystalline Al pillars with equivalent diameters, each containing a vertically-aligned grain boundary, is provided for comparison in the inset (reprinted with permission from Elsevier). In contrast to the compressive data generated for the slanted-boundary pillars in this work, stresses in the vertical-boundary samples exhibited significant hardening and pronounced stochastic behavior. (c) Post-deformation SEM image of the same pillar taken along the same directions as in (a), which shows that the upper grain sheared off from the lower grain along the grain boundary plane. Wavy features can be seen on the exposed grain boundary plane extending periodically from the near side of the pillar to the far side. Inset in the upper right corner shows a top-down view of the same pillar. All SEM images shown were taken at a 52° tilt angle between the sample surface normal and the electron beam.

The shear stresses acting along the grain boundary were calculated by resolving the measured applied axial stress onto the grain boundary plane in the direction of the offset. This corresponds to a $(111)/[01\bar{1}]$ system (in the upper grain with an axial orientation of $[3\bar{5}11]$), which has a Schmid factor of 0.372. This translates to a maximum resolved shear stress of 58 MPa and corresponds to the axial peak stress of 156 MPa at the strain of 0.5% and the average resolved shear stress of 36 MPa, computed by averaging over 120,000 data points between 2.4–16.2% strain. This maximum resolved shear stress is 39% lower than the shear stress at 7.5% strain resolved onto the principle slip system of 95 MPa reported for the bi-crystalline Al nano-pillars with a vertically oriented grain boundary [35]. The stiffness measured from the initial 15% of the data in the elastic unloading segment was 57 GPa, a value 25% lower than expected from theoretical calculations. The stiffness measured from tilted single crystalline pillars fabricated from grain 2 and did not contain a grain boundary was 66 GPa, a value within the range of measured stiffness seen in Al bi-crystalline pillars containing a vertical boundary [35]. The lower unloading stiffness measured for the pillars that deformed by sliding is likely a result of the reduced cross-sectional area as the top crystallite shears off, which may not be representative of the actual elastic modulus of the material.

4.2.2 Discussion

The first striking difference between the compressive stress-strain curves of the tilted-boundary pillars studied in this work and similar curves for the single crystalline and vertically oriented bi-crystalline samples is their continuous signature with almost negligible strain bursts. This is markedly different from the typical compressions of the single-crystalline and vertical grain boundary-containing bi-crystalline nano-metals, whose stress-strain signature is stochastic and populated with numerous strain bursts that range from 1 nm to ∼100 nm [2,59]. These bursts have generally been attributed to the initiation and propagation of avalanches of dislocations being released from their pinned locations and/or from dislocation sources [42,43]. The lack of such stochastic behavior and of noticeable crystallographic slip lines in the tilted-boundary nano bi-crystals suggests that when shear stresses are applied to the boundary, the deformation mechanism becomes distinctly different from the dislocation avalanche-driven plasticity.

The axial stress peaks at 156 MPa attained immediately after the elastic loading, which corresponds to a 58 MPa shear stress resolved onto the grain boundary plane in the direction of sliding, approximately a $(111)/[01\bar{1}]$ system. The observed subsequent softening is initially abrupt to $\sim$2.5% strain and is more gradual thereafter. This may physically correspond to the initiation of the shear offset at peak stress, followed by an abrupt drop in stress due to the inertia of the initial sliding and a deceleration at 2.5% strain, where the sliding becomes comparable to friction, and the deformation continues at a steady state. This sharp decrease in stress caused a momentary rise in the displacement rate, until the prescribed rate was re-established via the feedback loop algorithm in the nanoindenter software.

The primary slip system under compression for the upper grain (grain 1) is $(\bar{1}\bar{1}1)/[101]$, whose Schmid factor is 0.481. Although the boundary plane for grain 1 is of {111} type, the TEM image in Figure 4.3b reveals that it does not correspond to the primary slip system, which is denoted by the white arrow.

In the HRTEM image (Figure 4.3c), the set of parallel (111) planes align with the grain boundary, evidenced by the fringes in the upper grain. These planes terminate within the grain boundary and can be considered as ‘extra’ planes, or edge dislocations with a Burgers vector of $\sqrt{3}$. A lack of distortion of the fringes near the grain boundary suggests that little, if any, strain has accumulated in the vicinity of the boundary, likely due to the interrupted compatibility, or decohesion, between the crystallites after sliding.

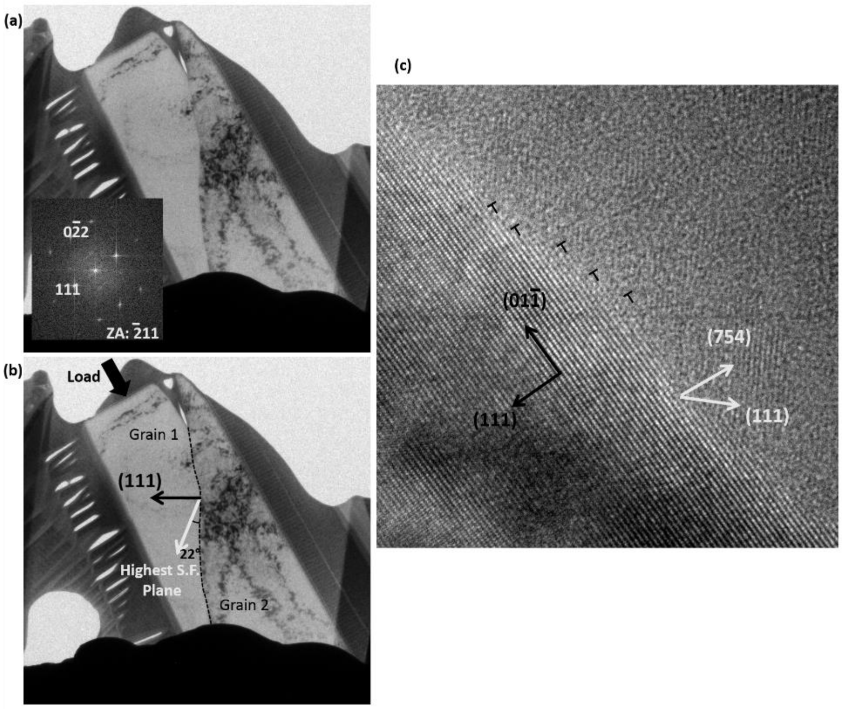

Figure 4.3: (a) TEM micrograph of the compressed pillar shown in Figure 4.2 . The diffraction pattern in the inset corresponds to the upper grain and was obtained by performing a Fast Fourier Transform on the HRTEM image shown in (c). A layer of amorphous Pt that was used to protect the pillar from FIB damage during TEM lamella preparation can be seen surrounding the pillar. (b) Same image as in (a) showing the loading direction, as well as the crystallographic orientations of the grain boundary plane normal of the upper grain and of the plane normal with the highest Schmid factor (denoted by the white arrow). (c) HRTEM of the grain boundary with in-plane directions labeled. The (111) planes in grain 1 terminate within the grain boundary and can be represented as an array of edge dislocations, each with a Burgers vector of $a/\sqrt{3}$, where a is the interatomic spacing.

Several experimental observations of grain boundary sliding in aluminum bi-crystals have been reported but only at elevated temperature [37,53,54,60]. Kegg et al. examined [011] symmetric tilt boundaries in Al that had been subjected to high-temperature (300–450 °C) shearing [52]. They attributed the sliding to the motion of grain boundary dislocations. From a dislocation reaction analysis, these dislocations were found to be lattice dislocations that were absorbed by the grain boundary and subsequently dissociated.

Such a coupled dislocation glide-climb behavior appears to be common in literature on high-temperature shearing of Al bi-crystals. Fukutomi et al. performed high-temperature, constant-load tensile creep test on Al bi-crystals containing a <110>Σ11 {113} symmetric tilt boundary [53] as well as boundaries that deviated slightly from the ideal orientation [60]. They observed that the deformation was dominated by the migration of the grain boundary with some sliding attributed to the movement of DSC (the lattice defined by the set of displacements that conserve the CSL lattice structure) dislocations. This intrinsic dislocation mechanism, glide coupled with migration, was also observed in hot-stage TEM along a near-Σ5 boundary [54].

It has also been suggested that for grain boundary dislocations that contained a Burgers vector parallel to the boundary plane, there would be a geometrically necessary step associated with them [61]. As a result, there is little chance that the boundary would deform by pure dislocation glide. The SEM images of the post-deformed samples in this work do not contain any evidence of boundary migration. The boundary itself remained planar throughout the deformation and its position within the pillar gauge section was unchanged. The homologous temperature of Al deformed at room temperature is ~0.3, a value half the temperature considered important for dislocation climb. In contrast to the described reports, all of which were performed at elevated temperatures, the experiments on the small-scale samples, each containing a single tilted high-angle boundary described in this work, were performed at room temperature. This suggests a markedly different deformation mechanism in these samples, one that is not thermally activated or facilitated.

To investigate the specific atomic-level processes governing grain boundary shearing, several molecular dynamics and first principles simulations on the structure and deformation of Al grain boundaries have been performed (for example, see review in ref. [62]). These computations were conducted mostly on the coincident site lattice (CSL) boundaries because of the straightforward mathematical formalism. The 0 K simulations by Molinari and Sansoz subjected a variety of symmetric tilt boundaries in Cu and Al to simple shear [63]. In that work, the most commonly observed sliding mechanism was via atomic shuffling at the boundaries, often accompanied by partial dislocation nucleation from the boundary into the adjoining lattices. Stress-strain data generated by these simulations was qualitatively similar to the experimentally observations in this work. These simulations also revealed a lack of the sudden atomic rearrangements at the boundary, a phenomenon found via the density functional theory simulations by Molteni et al [64]. MD simulations by Du et al. of high angle Al grain boundaries under simple shear at 750 K calculated critical stresses to induce grain boundary sliding to be as low as 20 MPa, and that the presence of vacancies decreased this critical stress [65]. While molecular dynamics simulations may be useful in understanding these experimental results, some do not account for effects of temperature and most are limited by their system size, computational cost, and unrealistic strain rates such that they may not be representative of the actual material behavior.

It is possible that some of the Ga ions may have segregated to the grain boundary during the FIB milling process, which would have contributed to the initiation of shear at the grain boundary, similar to the well-known liquid metal embrittlement of liquid Ga into grain boundaries of Al [66–70]. In these studies, an Al grain boundary is put in contact with a pure or saturated Ga liquid. The Ga then segregated to the Al grain boundaries, which resulted in an embrittlement of the material.

A report by Kiener et al., analyzed the damage induced by the FIB on Cu through the use of TEM and Auger electron spectroscopy [71]. Using a rectangular milling pattern, a voltage of 30 keV, and a milling time of 1000 s, they observe the maximum Ga concentrations to lie between 12 at% at 9 nm for the milling current of 10 nA and <2.0 at% at 3 nm for 50 pA.

The milling voltage used in this study was 30 kV and the current was iteratively reduced from 5 nA to 50 pA. The outer surfaces of the pillars were impacted by the ion beam oriented at a glancing angle, i.e., significantly below the amount of exposure, when the beam is aimed orthogonally at the sample, and the exposure times were no longer than 5 minutes for larger currents and typically less than a minute for lower currents. Therefore, it is reasonable to expect that the concentration of Ga on the outer surfaces of the Al samples studied in this work was substantially below the values reported by Kiener et al. The effect of Ga beam orientation on the fidelity and the mechanical properties of micro- and nano-mechanical samples was also discussed in Greer et al [72]. Another study by Hugo and Hoagland reported that the penetration velocities of Ga through the grain boundary ranged between 0.01–12.3 μms^{-1} depending on the grain boundary, but were typically less than 1 μms^{-1} [69]. The relatively larger pillars in our study, i.e., ones that were milled using higher currents and thus higher surface Ga concentration, would then be expected to have less penetration into the grain boundary because the material that was damaged in the course of previous milling steps was removed during each subsequent step. Hence, it is unlikely that the Ga effects from previous milling steps would increase the final Ga concentration significantly, and it is reasonable to expect the final surface concentration to be close to the 2.0 at% as reported above.

Schmid et al. studied Al alloys containing 0.4, 2.0, and 7.8 at% Ga and evaluated the Ga content at the grain boundary following thermal annealing at a range of temperatures [67]. These authors only observed Ga enrichment at the grain boundary for alloy concentrations of 2.0 at% or greater and only observed embrittlement for 7.8 at%. Using this argument, the estimated Ga concentration of 2.0 at% in this study would not result in embrittlement of the grain boundary.

Schmid et al. also estimated the Ga excess at the grain boundary to range between 0.6-1.9 monolayers in samples containing 7.8 at% Ga and 0.1–0.6 monolayers for 2.0 at% Ga [67] while Pereiro-López et al. report Ga film thickness on the order of 1 µm for grain boundaries exposed to saturated Ga liquid [66]. In contrast to these reports, we did not observe any such layer in our bright field TEM or HRTEM images shown in Figure 4.3. It is also unlikely that the full shearing-off of the top grain with respect to the bottom one observed in this work was caused by ion-induced embrittlement because the deformation was gradual, with substantial post-elastic flow in contrast to brittle failure [73]. Based on these arguments, we do not believe that Ga embrittlement is the sole source of the sample width-encompassing shear-off observed in the deformation of the Al nano-pillars studied in this work.

4.3 Analytic model of grain boundary sliding

The emergence of grain boundary sliding in the tilted boundary-containing nano-pillars compressed at room-temperature may be understood in terms of simple energy-balance arguments. From the post-deformation SEM images and the stress-strain data, it is clear that the upper grain sheared off and frictionally slid along the grain boundary. According to Griffith's crack and shear band propagation theory, the observed shear off-set can occur only if the recovered elastic energy is at least equal to the energy required to propagate it [74]. The elastic energy recovered during a single grain boundary sliding event over an axial distance d_{slide} can be represented by

$$\Delta E_{elastic} = \frac{Er^2\pi}{2h_o^2}\left[(d_{elastic} - d_{slide})^2(h_o - d_{elastic} + d_{slide}) - d_{elastic}^2(h_o - d_{elastic})\right] \quad \text{Eq. (4.1)}$$

where *E* is the elastic modulus, *r* is the radius of the pillar, h_o is the initial height of the pillar, and $d_{elastic}$ is the elastic component of the overall displacement, respectively. Figure 4.4a gives a schematic of the model geometry. The axial sliding distance, d_{slide} was determined by the time integration of the acceleration acting along the boundary plane. The acceleration due to the applied load and friction is

$$a = \frac{d_{elastic}E}{\rho h_o^2}(\cos\phi - \mu\sin\phi) \quad \text{Eq. (4.2)}$$

where ρ is the density of the material, μ is the coefficient of friction, and ϕ is the angle between the boundary and horizontal planes. The change in energy associated with creating new surfaces and with destroying grain boundary area, as the boundary planes are sheared past one another, is given by

$$\Delta E_{surface} = (2\Gamma_{surface} - \Gamma_{GB})\left[A(d_{plastic}) - A(d_{plastic} + d_{slide})\right] \quad \text{Eq. (4.3)}$$

where $\Gamma_{surface}$ is the surface energy of the exposed surfaces, Γ_{GB} is the grain boundary energy, and $A(d_{plastic} + d_{slide})$ is an analytic function, which represents the overlapping area of two ellipses translated relative to each other by a distance d_{slide} in a pillar of radius *r* and angle ϕ between the boundary and horizontal planes. The form of the area function is:

$$A(d) = \frac{2r^2}{\cos\phi} \cos^{-1}\left(\frac{d \cos\phi}{2r}\right) \qquad \text{Eq. (4.4)}$$

where *d* is a place-holder variable. We prescribed a displacement rate of 15 nm/s, a time step of 1.3 s and calculated the total change in energy at each step following Eq. 4.1-4.4. The condition for sliding to occur was:

$$\Delta E_{elastic} + \Delta E_{surface} < 0 \qquad \text{Eq. (4.5)}$$

If the above condition was not met, the pillar was loaded elastically until the following increment in strain. A schematic of this model with the parameters: $E = 66\ GPa, r = 500nm,\ h_o = 3\mu m, \Gamma_{surface} = 1.18\ Jm^{-2}, \Gamma_{GB} = 0.6\ Jm^{-2}, \phi = 55°, \rho = 270\ gmm^{-3}, \mu = 0.7$, is provided in Figure 4.4a, with the corresponding engineering stress, *σ*, normalized by the modulus, *E*, vs. engineering strain shown in Figure 4.5b. The values of $\Gamma_{surface}$, Γ_{GB} and *E* used here compare well with reported values of elastic modulus [35], grain boundary energy [75], and surface energy [76] of aluminum, although the density used is 5 orders of magnitude greater than the theoretical density. The impact of this discrepancy is discussed below, although the absolute choice of this value likely does not detract from the energetics-based argument.

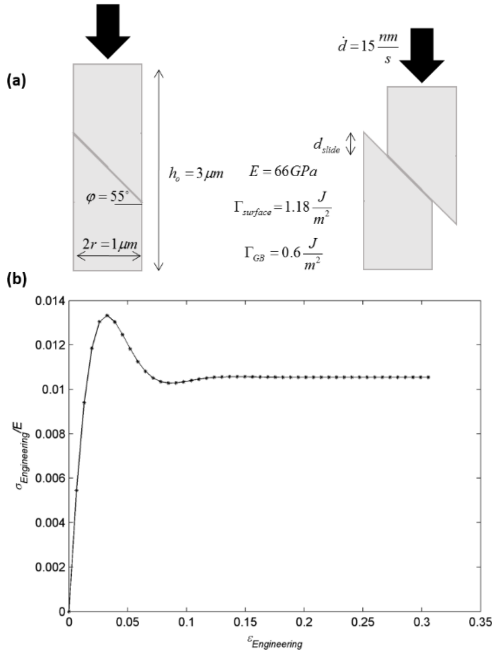

Figure 4.4: (a) Schematic of the sample geometry and frictional sliding used in the model. (b) Stress normalized by Young's modulus, E, vs. engineering strain. The maximum stress of 0.0133E is reached at the onset of grain boundary sliding corresponding to 3.3% strain after which the stress decreases to a local minimum of 0.0103E at 9.1% strain and eventually plateaus at 0.0106E.

The qualitative normalized stress-strain curve generated by following the described computational methodology is shown in Figure 4.5b. For the given values, the change in energy during the first time step is negative showing that sliding is energetically favorable at very low strains. Although the sliding mechanism is energetically favored from the beginning, the initial speed of sliding is low, and the stress-strain data is approximately elastic for the first few time steps before reaching peak stress. The stress then quickly decreases to a local minimum before increasing to a plateau when the sliding rate matches the displacement rate. This simple model appears to qualitatively capture three salient features observed experimentally: an initial peak, a subsequent local minimum, and a plateau. The source of these features is related to the velocity of sliding. Once sliding is initiated, the velocity of the upper crystal accelerates beyond the applied displacement rate, which corresponds to the quick softening after peak stress. Once a sufficient amount of elastic energy has been released, frictional deceleration brings the sliding rate to be slightly below the applied displacement rate, which results in a local minimum. The plateau region begins when the sliding rate is equal to the applied displacement rate. This signature is reminiscent of the phenomena of overshoot and ringing, features characteristic of damped motion. To further analyze the dynamic nature of these features, a quasi-static simulation was run where sliding was allowed to continue indefinitely as long as Eq. 4.5 was met. In such a case, the local minimum and plateau features were lost and the material showed only decreasing stress following the initial peak. The difference between the driving velocity and grain boundary sliding velocity as the source of the qualitative features in Figure 4.4b suggests that they are heavily rate dependent. Compression at a lower strain rate would then result in attenuation and eventual loss of these features.

Although this model is able to qualitatively capture the experimental stress strain response, it is simple and does not account for the physical complexity likely involved in the deformation. Alternate plasticity mechanisms such as creep and atomic rearrangements that may play a role in sliding are not considered here. The peak stress reached in the model is 1.3% percent of the prescribed elastic modulus compared to 0.27% in the experiment. Once softening begins, the model decreases to the local minimum by 29% from the peak stress followed by a 2.5% increase from the minimum compared to a decrease of 36% and increase of 13% seen in experiments.

In such a frictional sliding mechanism, a dissipation of energy through heat or other mechanisms would likely occur, which is not explicitly accounted for in Eq. 4.1– 4.4. Applying the no-friction condition in the computations results in a marked increase of several orders of magnitude in acceleration and no sliding. This shows that a significant amount of the loading acceleration lost is due to the opposing frictional forces. The direct effect of the increased density is a reduction in the acceleration in Eq. 4.2. Using the theoretical density results in a similar acceleration as seen when running the model without friction and no sliding. Both of these cases point towards the importance of the frictional term in dissipating energy and suggest that Eq. 4.2 is too simple an approximation of the dynamics and requires a more sophisticated implementation of friction. Despite these shortcomings, the qualitative agreement between some of the key features in the stress-strain curve generated by this analytical model is promising in gaining insight into understanding the mechanics and physics of grain boundary sliding in metallic nano bi-crystals.

4.4 Molecular dynamics simulations

4.4.1 Methodology

A 3D periodic bicrystal is generated using crystallite orientations obtained from experimental OIM data. Using an Al EAM potential [44], the total energy of the bicrystal is minimized to create the initial grain boundary configuration. The resulting bicrystal configuration was used for shearing simulations. For bicrystalline pillar compression simulations, the bicrystal was rotated at various angles and cylindrical geometry was cut from it resulting in a series of bicrystalline pillars with a GB plane normal inclined between 0° to 55° from the pillar axis. Pillars were 20 nm in diameter and 40 nm in length with the bottom of the pillar held fixed throughout deformation. Simulations were performed using the LAMMPS molecular dynamics software package [45] and visualizations were generated using OVITO [47]. Figure 4.5a shows the initial grain boundary-containing nanopillars.

Pillar compression was induced by simulated indentation. A planar indenter was inserted into the simulation box and applied against the top of the pillar. Simple shear was induced by translating a 2 nm thick block of atoms located 8 nm from the GB at constant velocity parallel to the GB. A similar 2 nm thick block of atoms located 8 nm below the GB was held fixed. Directions parallel to the GB were held under normal stress-free boundary conditions during straining. The local crystalline structure of each atom was calculated using the common neighbor analysis method through the OVITO software. Figure 4.7a shows a side view of the initial grain boundary configuration. We refer to the upper grain as Grain 1 and the lower grain as Grain 2.

Indenter and shearing velocity were chosen to result in a strain rate of 10^8 s^{-1}. Stress was calculated via Equation 3.1 every 0.1 ps up to 10% engineering strain.

4.4.2 Results of compression and shearing simulation

Figure 4.5b shows a summary of force data generated from compression simulations of bicrystalline nanopillars with a high-angle grain boundary at inclination angles between 0° to 55°. All simulations were performed at 300K. For an inclination of 0°, the force increases linearly, followed by a significant drop in force and reloading. This signature corresponds to elastic loading followed by dislocation nucleation and is typical of single crystalline nanopillar/nanowire MD simulations [38,77]. Figures 4.5a and 4.5c show the simulation nanopillar before and after deformation, where it is seen that for an inclination angle of 0° the grain boundary has not deformed significantly.

Compression on bicrystals with inclination angles from 15° to 55° all show force data that differs significantly from an inclination angle of 0°. The forces are much lower than those seen in the 0° simulations and there is no dramatic drop in force associated with a nucleation event. After an initial linear increase, the force remains relatively constant throughout the simulation with low-magnitude oscillations. Comparing the pre- and post-deformation models of the simulated nanopillar, it’s seen that grain boundary sliding was the dominant deformation mechanism.

Figure 4.6a shows simulations performed on a nanopillar containing a single high-angle grain boundary inclined 45° from the pillar axis at various temperature ranging from 10K to 500K. The generated force data is qualitatively similar, showing linear loading followed by yielding and a post-elastic signature displaying continuous, oscillating force with low hardening. In contrast to expected monotonic softening with increasing temperature, 300K and 500K simulations show increased strengths and hardening behavior above the 100K and 10K simulations, respectively. Figure 4.6b presents cross-sections of the deformed nanopillars colored by their centro-symmetric value. No dislocation structures are observed in either crystal. At 300K and 500K, grain boundary sliding is accompanied by curvature and migration of the grain boundary at the free surface.

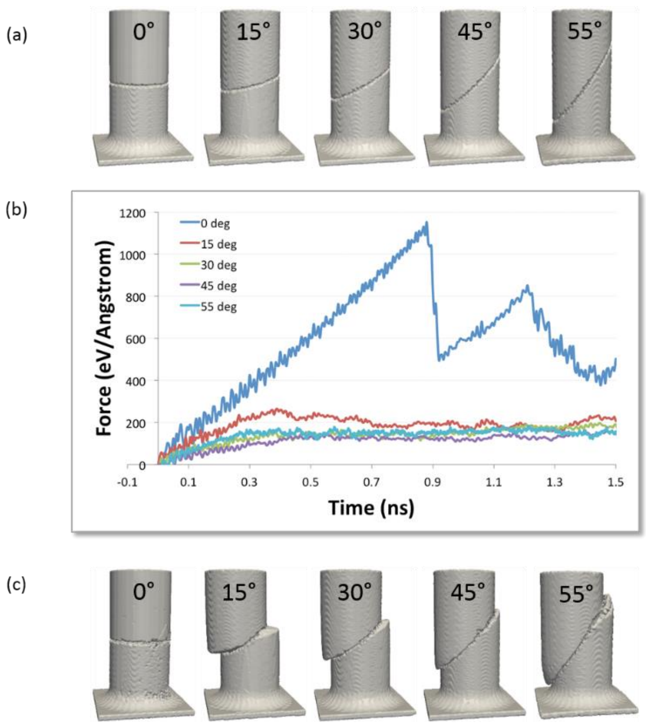

Figure 4.5: (a) Initial configuration of nanopillars containing a GB at various tilt angles for MD simulations. (b) Generated stress-strain data for compression of bicrystals shown in (a). (c) Final deformed configuration of bicrystalline nanopillars.

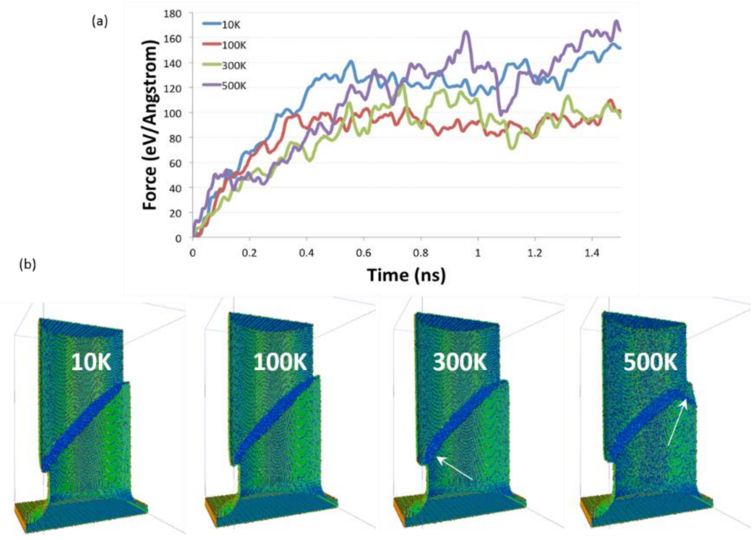

Figure 4.6: (a) Compressive stress-strain data for a bicrystalline nanopillar containing a single GB tilted 45° from the axis of compression. Curves correspond to simulations performed at various temperatures.

(b) Cross-section views of deformed bicrystals at various temperatures. Atom are colored by their centrosymmetric value and FCC atoms are removed. Curving/migration of the grain boundary near the free surface is observed in both the 300K and 500K simulations, as indicated by the arrows.

Figure 4.7b shows the combined engineering stress strain data generated for the planar grain boundary shearing simulations. Yield and flow stresses decrease with increasing temperature up to 300K. At 500K, the flow stress increases near values seen in the 100K simulation. The post-yield stress signature in simulations from 10K to 300K is characterized by high-frequency oscillations and decreasing hardening with temperature. In the 500K simulations, high-frequency oscillations are not present, but stress is characterized by long-period oscillations and near-constant flow stress.

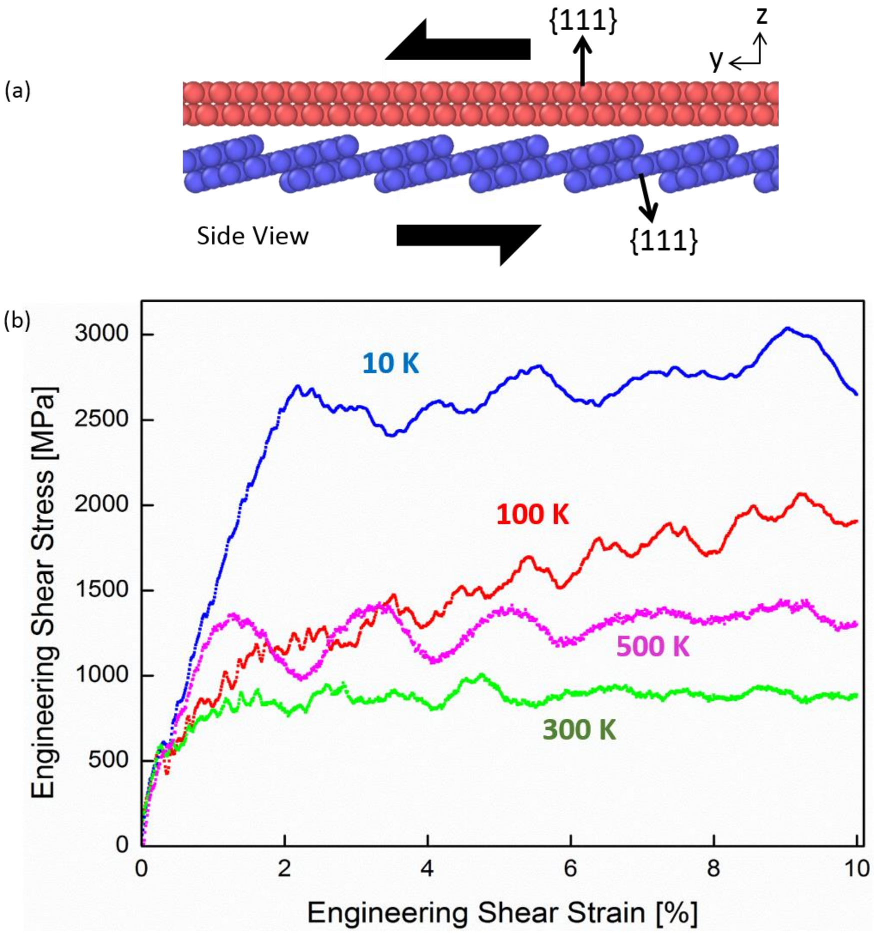

Figure 4.7: (a) Side view of initial planar grain boundary. Grain 1 (top crystal) is oriented with {111} planes parallel to the grain boundary. {111} planes of Grain 2 (bottom crystal) terminate in the grain

boundary. (b) Stress-strain data generated from shear MD simulations of the planar boundary given in (a) at various temperatures.

4.4.3 Discussion

Snapshots from the 0° nanopillar simulation show that deformation is accommodated by heterogeneous dislocation nucleation that precipitates the large drop in force. No significant deformation of the grain boundary was observed in the 0° nanopillars. The force data generated from these simulations is similar to stress-strain signatures of previous nanopillar simulations where deformation was dislocation dominated [38,77]. With increasing tilt angle, we observe a transition in the force data and the nanopillar morphology. Force signatures are continuous and oscillatory and deformation snapshots show grain boundary sliding and the absence of dislocation nucleation.

For compression of a nanopillar containing a grain boundary tilted 45° from the axis, grain boundary sliding is observed at all temperatures. The unexpected hardening observed at 300K and 500K may be related to the observed curvature and migration of the grain boundary at the intersection of the grain boundary and free surface. Increasing curvature of the grain boundary will require increasingly higher stresses to continue sliding. In the planar shearing simulations, there is a similarly unexpected increase in flow stress between the 300K and 500K and no dislocation activity is observed in any planar shearing simulation. Because these simulations are performed in the absence of a free surface and no internal deformation structures are observed, this suggests that the stress-strain signatures in the nanopillar simulations are in part determined by the elastic shear state of the crystals in addition to potential hardening caused by boundary curvature.

Figure 4.8a shows the combined stress-strain data and atomic migration information for the 10K shearing simulation. Note that atomic radius has been decreased to highlight the lattice plane configurations and individual atomic positions. We define the net atomic migration as the number of atoms that migrate from Grain 1 into Grain 2 subtracted by the number of atoms that migrate from

Grain 2 to Grain 1. Figure 4.8b gives several snapshots of the grain boundary during deformation and shows their corresponding location on the stress-strain plot. At snapshot I, shearing is elastic and no grain boundary sliding is observed. The boundary cross-section shows that some atoms from the top crystallite have migrated to the bottom crystallite as indicated by atoms colored white. This occurs during energy minimization where {111} facets from Grain 2 provide energetically-favorable sites for Grain 1 atoms to relax into. When grain boundary sliding begins at snapshot II, we see Grain 2 atoms begin to migrate to Grain 1, indicated by atoms colored black. The cross-section at snapshot III shows that after large grain boundary sliding, there is a net increase in atoms that have migrated from Grain 1 to Grain 2, yet the grain boundary structure has not changed significantly from the initial configuration. We observe similar migration occurring in the 100K and 300K simulations, but the greater available thermal energy makes atomic migration easier and the resulting net migration decreases with temperature.

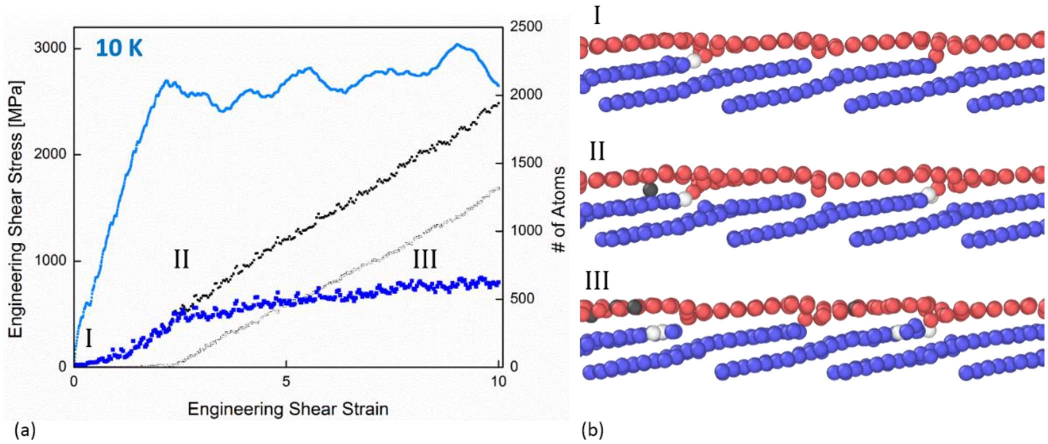

Figure 4.8: (a) Combined stress-strain data and net atomic migration data for 10K shearing simulation. Grain boundary sliding activates when Grain 2 atoms begin migrating into Grain 1. (b) Cross-section snapshots of 10K planar grain boundary at various stages of shearing. White atoms indicate atoms that have migrated from Grain 1 to Grain 2 and black atoms indicate atoms that have migrated from Grain 2 to Grain 1.

(a)

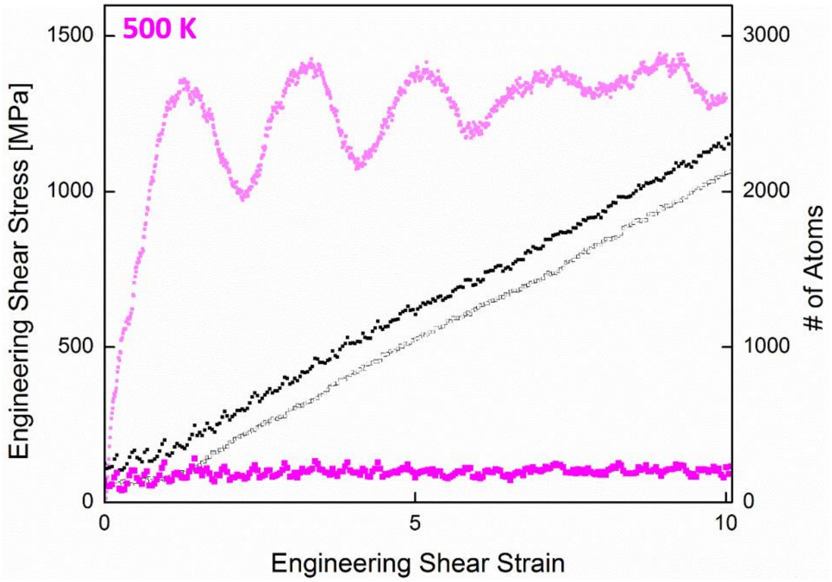

(b)

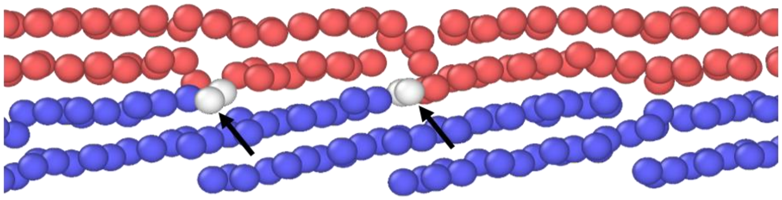

Figure 4.9: (a) Combined stress-strain data and net atomic migration data for 500K shearing simulation. Net atomic migration stays constant throughout shearing. (b) Cross-section view of 500K planar grain boundary. Arrows indicate points where {111} planes of Grain 2 have extended to join with {111} planes of Grain 1, effectively extending the grain boundary locally into Grain 1.

The above atomic behavior can be associated with strengths and high-frequency oscillating features observed in the 10K, 100K, and 300K simulations, but cannot explain the stress-strain signature of the 500K simulations. Figure 4.9a shows the combined stress-strain and atomic migration data for the 500K simulation. We see that migration of atoms between grains begins immediately and remains constant throughout the simulation. The deformed cross-section in Figure 4.9b shows that in contrast to the low temperature simulations where the grain boundary morphology did not change, reconfiguration at the grain boundary occurs during energy minimization. The {111} planes from the Grain 1 curves down to join the {111} planes in Grain 2, effectively extending the grain boundary locally into Grain 1. These local asperities increase the required stress for grain boundary sliding despite greater kinetic energy facilitating more atomic migration.

4.5 Summary

In summary, we investigated the mechanical response of uniaxially compressed 900 nm-diameter aluminum bicrystals, each containing a high-angle grain boundary with a plane normal inclined at 24° with respect to the loading direction. We observed frictional grain boundary sliding at room temperature, where the top crystallite is sheared off as a single unit along the grain boundary. A typical compressive stress-strain data showed an initial peak of 156 MPa after elastic loading, that corresponds to 58 MPa resolved onto the grain boundary plane and in the direction of slip, a value 39% less than the critical resolved shear stress for bi-crystalline Al nano-pillars with a vertically oriented grain boundary [35]. This was followed by a sudden softening to 100 MPa at 2.5% strain. The stress then varied continuously between 79–112 MPa for the remainder of compression up to an unloading strain of 16.2%. No strain bursts were observed in the compression data. Post-deformation SEM images conveyed that nearly all plastic deformation was carried by a single shear offset along the grain boundary. TEM analysis revealed the grain boundary plane of the upper crystalline to be {111} type, which does not correspond to the primary slip system under compression. HRTEM images revealed that {111} planes were approximately aligned with the grain boundary and terminated within the boundary as extra atomic half-planes, i.e., edge dislocations. To better understand frictional grain-boundary sliding at room-temperature, we developed a simple physical model based on the energy-balance. This model simulates dynamic frictional sliding under the constraint that the created surface energy must be compensated by the recovered elastic energy. The stress-strain data generated by this model are able to qualitatively capture the three important features seen experimentally (an initial peak, a subsequent local minimum, and decreased flow stress) and suggest that the mechanism of sliding is frictional in nature.

Molecular dynamics simulations on compression of bicrystalline nanopillars containing a single grain boundary with an inclination angle between 0° to 55° from the pillar axis show a transition from dislocation-dominated deformation to grain boundary sliding. At 300K and 500K, the free surface allows for curvature/migration of the grain boundary and contributes to higher forces required for sliding. Planar shearing simulations reveal that grain boundary sliding is accommodated by atomic migration and that net atomic migration is associated with increasing stresses during sliding. At 500K, we observe similar increases in strength as observed in nanopillar compression simulations, but attribute strengthening to local extension of the grain boundary into Grain 1. This combination of experiments and simulation suggests that the frictional grain boundary sliding may be the dominant deformation mechanism in nano bi-crystals when a shear stress is present across the boundary.

5. Effect of Size, Orientation, and Alloying on the Deformation of Single Crystalline Magnesium (AZ31)

Research was sponsored by the Army Research Laboratory and was accomplished under Cooperative Agreement Number W911NF-12-2-0022. The views and conclusions contained in this document are those of the authors and should not be interpreted as representing the official policies, either expressed or implied, of the Army Research Laboratory or the U.S. Government. The U.S. Government is authorized to reproduce and distribute reprints for Government purposes notwithstanding any copyright notation herein.

5.1 Introduction

There has been an increasing demand for lightweight materials in the automotive and aerospace industries, which resulted in renewed surge of interest in Mg and its alloys. As early as the 1920's Mg-alloys were utilized in airplane engines and racecar components [78,79] for their light weight and favorable strength [80–83]. In addition to being the lightest structural metal, Mg has been shown to exhibit excellent fatigue resistance [84] and high damping capacity [85], but its poor formability and limited ductility have prevented the development of production processes for component parts. This low ductility at room temperature is caused by the inherent anisotropy and a shortage of available slip systems in hexagonal close-packed (HCP) materials. For pure Mg at room temperature, dislocation slip in the basal crystallographic planes is the dominant deformation mechanism. This provides only two independent slip systems for deformation, whereas five are required to carry out homogeneous deformation, as specified by the von Mises criteria [86].

Several methods have been pursued to improve the ductility of Mg, for example alloying and texture control [87–89]. For the mechanisms that lead to enhanced ductility in the alloys are thought to be an elevated activity of non-basal slip systems through a decrease in the Peierls stress, but the evidence of such easing of non-basal slip in single crystalline alloys has been limited to prismatic slip in tension of a small selection of binary alloys [88]. Developing a thorough understanding of the mechanical properties and deformation mechanisms in Mg and its alloys is of fundamental importance. Of particular interest are alloys utilizing Al and Zn, designated by convention as the “AZ” alloys, with the subsequent number referring to the weight percent of the alloying elements. A lack of experimental data, which describes deformation of single-crystalline AZ31 (3% wt. Al, 1% wt. Zn) alloy, including the elastic moduli and the critical resolved shear stresses, as well as an understanding of the underlying dislocation mechanisms, presents an impediment to help guide the development of improved Mg alloys. In part, such a shortage of data stems from the lack of availability of single crystals of AZ31 able to be used in conventional macro-scale mechanical testing. Hot rolling and extrusion are the preferred processing method because of the resulting fine-grained microstructure.

The grain size in a typical AZ alloy after extrusion can vary between 2 and 23 µm depending on extrusion conditions [90,91]. Nano-scale uniaxial compression experiments then offer a useful methodology to test single-crystalline Mg alloy samples in a variety of known crystallographic orientations. The anisotropy of the slip systems and challenges associated with sample preparation have rendered HCP crystals a less explored material system for nano-plasticity testing in contrast to face-centered cubic (FCC) and body-centered cubic (BCC) metals; for example, Mg is also known to deform via twinning, which can make the mechanical response difficult to interpret. A key finding in virtually all uniaxial compression studies on micro and nano-sized single crystalline metals is the emergent dependence of the flow stress on sample dimensions, with smaller generally being stronger for single crystals [1,2]. Face-centered and body-centered cubic materials follow a power law scaling behavior, with an average exponent of ~0.6 for FCC materials. It should be noted that the exponent is also a strong function of the initial dislocation density [10,92]. Recently, attention has been directed towards identifying the effect of crystal size and orientation on the deformation mechanisms and mechanical properties of pure Mg microcrystals [93–98] using the micro-tension and/or micro-compression experimental technique [99]. Hexagonal close-packed materials also appear to follow a scaling law, but with a lack of data the scaling behavior is less clear [1]. Clearly, further investigation is required into the nano-scale mechanical behavior of HCP metals to reach the same level of understanding we have of cubic metals.

Byer et al. performed uniaxial compression experiments on micron-sized Mg single crystals where the loading direction was parallel to the c-axis of the crystal [93]. These single crystals were fabricated in a cylindrical geometry with diameters ranging between 2.5-10 µm. The authors reported the activation of the pyramidal slip planes and significant hardening under compression up to 12% strain. No deformation twinning was observed. Across the sample sizes of 2.5 to 10 microns utilized in this study, virtually no size effects were observed, which was hypothesized to stem from the very high dislocation densities present in these crystals. The same authors investigated the effect of initial dislocation density of the mechanical behavior of single crystalline Mg pillars, whereby samples with diameters of 600 nm - 10 µm were prepared and uniaxially compressed along [0001] and $[2\bar{3}14]$ axis [96]. The initial dislocation density was controlled by fabricating compression pillars from samples that contained a deformation layer introduced during mechanical polishing prior to fabrication and from samples where this deformed layer was etched away. Pyramidal slip was reported for samples compressed parallel to the c-axis, with no deformation twinning. Basal slip was the preferred deformation mechanism for samples compressed along the $[2\bar{3}14]$ axis. A power-law size effect was observed in the samples with a low initial dislocation density of (1.1±0.18) x 1013 m^{-2} in both orientations, which was suppressed when the dislocation density was increased to (3.0±0.5) x 1013 m^{-2}. Lilleoden also performed micro-compression tests along the (0001) axis of single crystalline Mg micropillars with diameters ranging between 2.1 to 10 µm [94]. A size effect and pyramidal slip with no deformation twinning was reported.

On the other hand, Ye, et al. conducted uniaxial compression experiments on pure Mg and Mg-0.2% Ce alloy in an in-situ TEM [95]. These authors observed a significant size effect for samples with diameters between 200 nm to 1.6 µm in all tested orientations. When compressed along the $[3\bar{9}4]$ axis, basal slip dominated deformation. In contrast to previous reports, extension twinning was reported in both Mg and Mg-0.2% Ce when deformed along the [0001] axis. A decrease to 15% of the critical resolved shear stress of pure Mg was reported for Mg-0.2% Ce alloy samples.

Following this work, Yu, et al. performed in-situ TEM compression, tension, and bending experiments such that the [0001] direction was always parallel to the loading direction [99]. Samples were square in cross-section, with side lengths of 150 nm. The nucleation and growth of a single contraction twin was observed in compression, while an array of nano-twins was formed as a result of tension along the same axis.

Kim performed uniaxial compression on pure Mg parallel to the [0001], $[2\bar{1}\bar{1}2]$, $[10\bar{1}1]$, $[11\bar{2}0]$, and $[10\bar{1}0]$ directions [97,98]. Single crystal samples varied in diameter between 1 to 10 µm. Compression parallel to the [0001], $[2\bar{1}\bar{1}2]$, and $[10\bar{1}1]$ axes resulted in deformation by dislocation slip. In contrast, deformation twinning and dislocation slip during compression along the $[11\bar{2}0]$ and $[11\bar{2}0]$ directions was observed. The flow stress in [0001], $[2\bar{1}\bar{1}2]$, $[11\bar{2}0]$, and $[10\bar{1}0]$-oriented samples was observed to follow a power-law increase with decreasing pillar diameter. The power-law exponent was also seen to depend on the sample orientation with twinning dominated orientations showing larger exponent amplitudes.

This review of the existing experimental data on deformation of small-scale Mg and Mg-alloys can be summarized as follows:

(1) Virtually all existing reports focused on pure Mg, with the most common experiment being uniaxial compression along the c-axis.

(2) A wide range of phenomena have been reported, especially pertaining to deformation twinning, with no unified understanding on slip vs. twinning.

(3) The size-strength dependence was reported to vary among authors and orientations, but the influence of orientation on the size effect remains unresolved.

This summary demonstrates that the current understanding of small-scale deformation of Mg and Mg-alloys is incomplete and results remain inconclusive. Systematic investigations are necessary, particularly on the effect of orientation and alloying.

We present a set of systematic uniaxial compression experiments and microstructural characterization of single crystalline AZ31 alloy (Mg-3.0% Al-1.0% Zn) on small-scale cylindrical samples with diameters ranging between 300-5000 nm. We performed compressions along two distinct families of expected deformation mechanisms: (1) along [0001], which is expected to deform via pyramidal slip or compression twinning and (2) along multiple planes misoriented from the c-axis by 22-69°, which are expected to deform via basal slip.

We also employed three-dimensional (3D) discrete dislocation dynamics (DDD) simulations to identify the dislocation mechanisms controlling the size-affect response of Mg microcrystals and to further investigate their orientation dependence. All 3D-DDD simulations in this study were performed using the Multi-scale Dislocation Dynamics Plasticity (MDDP) code originally developed by Zbib et al. [100,101] to model dislocation glide in FCC single crystals. Simulations were performed on samples with the compression axis parallel to the [0001] and $[11\bar{2}2]$ crystallographic directions, orientations expected to deform by pyramidal and basal slip, respectively.

Experimentally we observed two distinct stress-strain signatures and deformation characteristics with no observable deformation twinning. 3D-DDD simulations showed a dependence of stress-strain signature and attained stresses on orientation that is in qualitative agreement with experiments. A unique size effect was present in each crystallographic orientation in both experiments and simulations, each following the “smaller is stronger” trend. We show that the mechanism controlling the size effect in both orientations is the activation of the weakest source and that the anisotropy in intrinsic lattice resistance gives rise to a difference in scaling exponents. This implies that in the AZ31 alloy, the deformation at the submicron length-scale is dominated by the size effect rather than by solid solution strengthening through alloying. We discuss these findings in the framework of small-scale plasticity and crystallographic slip mechanisms.

5.2 Methods

5.2.1 Surface preparation, characterization and sample fabrication

Bulk samples of AZ31 were first prepared from wrought alloys using equal channel angular extrusion (ECAE) following route 4BC. This process involved extruding the material through a 90° angular channel a total of 4 passes, rotating the billet 90° about its axis after each extrusion at 200 °C and 1240 psi. Several smaller cubic pieces of 1 cm^3 were then extracted using electron discharge machining (EDM).

A chosen surface of one of the cubic AZ31 blocks was then mechanically polished using abrasive lapping pads embedded with aluminum oxide (Al_2O_3) particles. Pads with successively finer particle sizes were used to polish the surface down to a final 3 µm particle size.

Mechanical polishing was followed by electrolytic polishing in a solution of ethanol and phosphoric acid (85%) in a volume ratio of 5:3. A polishing mask was used to expose an area of 0.25 cm^2 of the metal surface to the electrolyte. Electro-polishing was performed using a voltage of 2 V, and the polishing solution was maintained at a temperature between 0-5 °C throughout the process. After polishing for 2-3 minutes, the sample was immediately removed from the polishing table and immersed in methanol. Gentle agitation followed by sonic cleaning fully dissolved the white film that formed on the surface during polishing. The sample was then allowed to dry in air and typically yielded a mirror finish. Figure 5.1b shows a SEM image of the polished surface. Polishing at higher temperatures, for longer times, or failure to immediately immerse in methanol always resulted in the formation of a dull, porous surface oxide layer. Figure 5.1a shows a TEM micrograph of this surface layer. Energy dispersive spectroscopy (EDS) data shows a high concentration of phosphorous from the electrolyte localized in this layer. The thickness and surface coverage of this oxide appeared to increase with temperature and polishing time. This surface oxide could be removed using a buffered hydrofluoric acid etch and yielded a smooth surface, but the surface quality degraded after 2-3 days.

Electron backscatter diffraction (EBSD) was used to characterize the size and orientation of grains. Presence of a surface oxide layer from poor sample preparation resulted in an inability to obtain a clear Kikuchi pattern from the bulk. Figure 5.1c shows an Orientation Imagining Microscopy (OIM) crystallographic map generated based on the polished surface after a thermal anneal in vacuum at 450° C for 5 hours. Processing using Oxford's Channel 5 software revealed a strong basal texture ~80° from the extrusion direction and an average grain size of 2.5±1.6 µm before thermal annealing. This grain size is consistent with other reports for AZ31 processed via ECAE under similar conditions [91], but is too small to guarantee that the compression samples fabricated using the FIB will be single crystalline. Thermal annealing at 450° C for 5 hours increased the average grain size to 11.5±9.6 µm [102].

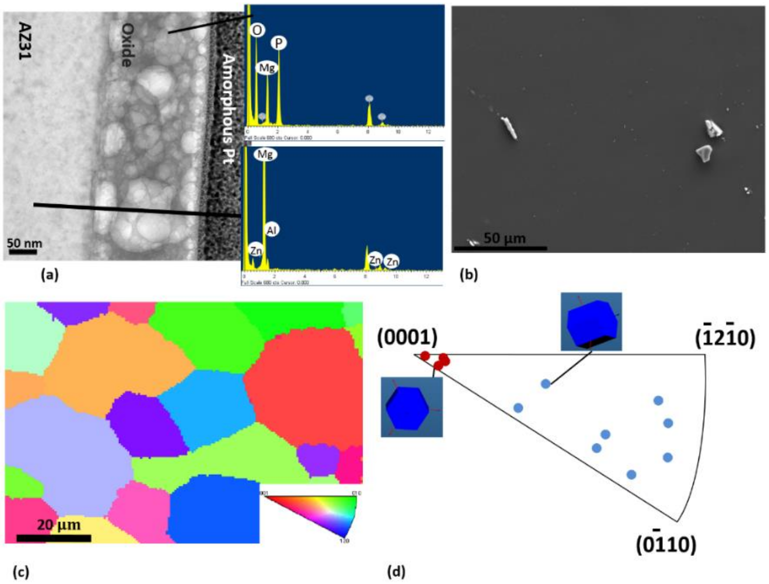

Figure 5.1: (a) TEM micrograph showing a porous oxide covering the AZ31 surface. This was observed during electro-polishing at elevated temperatures or if the sample was not immediately cleaned following polishing. The amorphous layer of Pt was used as protection during the TEM sample preparation process. (b) SEM image of the smoothed sample surface following electro-polishing. Al-Mg precipitates ranging approximately 1 to 10 μm can be seen partially and fully embedded in the AZ31 matrix. (c) Orientation Imaging Microscopy map generated by EBSD showing grain structure of annealed and polished surface with average grain size of 11.5±9.6 μm. (d) Stereographic triangle showing the grain orientations that were used to fabricate compression samples.

Cylindrical compression samples were fabricated using the FIB and the top-down methodology [5,8,42,57,58]. The specific grains for sample extraction were chosen such that the surface was parallel to one of two crystallographic orientations, (0001) or tilted acutely away from the c-axis. Figure 5.1d shows a stereographic triangle and gives the orientations of the grains used to fabricate compression samples. The fabrication was accomplished by placing concentric annular patterns into the field of view on the ion-beam image and progressively milling away material until the final inner pattern diameter of 300-5000 nm. The aspect ratio (height/diameter) was maintained between 3:1 and 4:1. Sample diameters were calculated by taking the average of the diameter measured at the top of the pillar height and the bottom of the pillar height. A SEM image of a representative single-crystalline sample after deformation is shown in Figure 5.2b.

Uniaxial compression experiments were performed in a nanoindenter (Triboscope, Hysitron Inc.) using a diamond flat punch tip with a diameter of 8 μm. Tests were conducted under displacement rate control, at the nominal strain rate of 10^{-3} s^{-1} up to a total strain between 8-15%. The displacement was monitored continuously at a frequency of 78 kHz via a feedback loop through the Hysitron performec control module. Engineering stress and strain were calculated by dividing the force and displacement by the initial cross-sectional area and pillar height, respectively. Resolved shear stresses were determined using the maximum Schmid factor for each slip system calculated from the crystal orientation obtained from OIM analysis. Bunge Euler angles $\{\phi_1, \theta, \phi_2\}$ were first converted to their corresponding Miller-Bravais [hkil] direction values using [103]:

$$\begin{bmatrix} h \\ k \\ i \\ l \end{bmatrix} = \begin{bmatrix} \frac{\sqrt{3}}{2} & -\frac{1}{2} & 0 \\ 0 & 1 & 0 \\ -\frac{\sqrt{3}}{2} & -\frac{1}{2} & 0 \\ 0 & 0 & \frac{c}{a} \end{bmatrix} \begin{bmatrix} \sin\varphi_2 \sin\theta \\ \cos\varphi_2 \sin\theta \\ \cos\theta \end{bmatrix} \tag{Eq. (5.1)}$$

where c/a is the ratio between the length of the c-axis and the in-plane lattice constant within the unit cell and is 1.624 for Mg. The vector on the right hand side of Eq. 5.1 corresponds to the z-component of a Bunge rotation of an orthonormal coordinate system and the matrix transforms the orthonormal system to the Miller-Bravais basis. The 4-index Miller-Bravais notation of a given deformation system, {hkil}/<uvtw>, can be converted to 3-index hexagonal Miller notation by [104]:

$$[h_1 \quad k_1 \quad l_1] = \left[h - i \quad k - i \quad \tfrac{3}{2}\left(\tfrac{a}{c}\right)^2 l\right] \tag{Eq. (5.2)}$$

$$[u_1 \quad v_1 \quad w_1] = [u - t \quad v - t \quad w] \tag{Eq. (5.3)}$$

Note that in the hexagonal system a direction is not necessarily normal to a plane of the same indices and so the deformation plane must first be converted to its corresponding direction normal as seen in Eq. 5.2. The direction cosine between the loading direction and the deformation plane normal direction, $\cos\varphi$, and the direction cosine between the loading direction and the slip direction, $\cos\lambda$, are calculated as:

$$\cos(\varphi \ or \ \lambda) = \frac{u_1u_2 + v_1v_2 - \frac{1}{2}(u_1v_2 + u_2v_1) + \left(\frac{c}{a}\right)^2 w_1w_2}{\sqrt{\left(u_1^2 + v_1^2 - u_1v_1 + \left(\frac{c}{a}\right)^2 w_1^2\right)\left(u_2^2 + v_2^2 - u_2v_2 + \left(\frac{c}{a}\right)^2 w_2^2\right)}} \tag{Eq. (5.4)}$$

where $[u_2 \quad v_2 \quad w_2]$ is the loading direction and $[u_1 \quad v_1 \quad w_1]$ is the deformation plane normal direction (or the deformation direction). The Schmid factor, M, then has the common meaning of:

$$M = \cos\phi \cos\lambda \tag{Eq. (5.5)}$$

Yield stresses were determined by the stress at the first significant strain burst event. This event can be identified by a sudden increase in the velocity of the indenter tip that results in a discontinuity in the data. This increase varied among samples, but was typically 4-5 standard deviations above the average tip velocity. If no bursts were present in the data, a 0.2% offset method was utilized with a slope approximated from a region on the loading curve after the initial non-linear segment when the tip is not in full contact with the pillar head.

Analysis of microstructure in the polished material and deformed samples was performed via transmission electron microscopy (FEI, Tecnai F30) at an accelerating voltage of 300 kV. Samples were lifted out from the bulk polycrystal using a micro-manipulator (Omniprobe, Inc.) within the SEM and attached to a TEM grid with ion-beam assisted, site-specific, Pt deposition. Once attached to the TEM grid, the samples were thinned using decreasing current down to 10 pA to a thickness of <100 nm to ensure electron transparency.

5.2.2 Discrete dislocation dynamics simulations

To allow for the simulations of dislocation ensembles in HCP microcrystals, the slip planes and Burgers vectors of the HCP lattice (summarized in Table 1 [105]) were introduced into MDDP. The experimentally measured Peierls stresses for dislocations on the basal, prismatic, and pyramidal planes, which equal 0.52 [106], 39.2 [107], and 105 MPa [108], respectively, were introduced into the code. These values also agree with molecular dynamics (MD) simulations on these slip systems [109,110]. Since cross-slip in HCP crystals is not yet fully characterized in literature, the current simulations did not consider this possible deformation mechanism. Two orientations were simulated, namely microcrystals oriented for compression along the c-axis $[0001]$, and along the $[11\bar{2}2]$ directions. In the $[11\bar{2}2]$ orientation, the c-axis makes an angle of 45° with respect to the loading axis.

Table 1. Slip planes and Burgers vectors used in the present DD framework [103].

Slip planes	Basal – {0001}	Prismatic – $\{10\bar{1}0\}$		1st Order Pyramidal – $\{10\bar{1}1\}$		2nd Order Pyramidal II – $\{11\bar{2}2\}$
Burgers vectors	⟨*a*⟩ ≡ $< 11\bar{2}0 >$	⟨*a*⟩ ≡ $< 11\bar{2}0 >$	⟨*c*⟩ ≡ ⟨0001⟩	⟨*a*⟩ ≡ $< 11\bar{2}0 >$	⟨*c+a*⟩ ≡ $< 11\bar{2}3 >$	⟨*c+a*⟩ ≡ $< 11\bar{2}3 >$

All simulated microcrystals had a rectangular shape with a squared cross-section having an edge length, D, varying between 0.5 and 1.0 µm, and a fixed aspect ratio of h/D = 2.5. The microcrystal bottom surface was constrained in all directions (i.e., $u_x = u_y = u_z = 0$), and a displacement-controlled compressive load was applied on the top surface such that $u_z = \varepsilon h$ [111]. The nominal strain rate was fixed in all simulations at $\dot{\varepsilon} = 1000\ s^{-1}$, which is higher than that in experiments to reduce the computation cost [111]. The drag coefficient for pure screw dislocations was set to $B_{screw} = 10^{-1}\ Pa\ s$, and for non-screw dislocations $B_{non-screw} = 10^{-4}\ Pa\ s$ [43]. The initial dislocation density in all simulations was $\rho_{src} = 6x10^{12} m^{-2}$, with a random dislocation length, l_{src}, between 0.19-0.32 µm (i.e., mean length is 800*b*). 8 realizations for each microcrystal size and orientation with different initial random dislocation distributions were simulated. To account for the anisotropy of the HCP lattice, the shear modulus along the c-axis was 22.4 GPa, along the basal slip is 12.7 GPa, and the Poisson ratio is *v* = 0.34 [97]. Finally, the mass density 1738 kg m^{-3}, the Burgers vector magnitude for <a> dislocations was *b* = 0.32 nm, and the *c/a* ratio = 1.624, were all inputs to the DDD simulations.

From the current experiments, as well as others published in literature, dislocation-mediated plasticity was observed to be the dominant deformation mechanism in micron and submicron crystals, and no twinning has been observed [93–97]. However, for microcrystals having sizes below 250 nm, twining reoccurs under c-axis compression loading [99]. Thus the DDD simulations performed here, which account only for dislocation evolution, can effectively model the deformation mechanisms in microcrystals larger than 250 nm. In addition, we have performed preliminary simulations with dislocations on all four slip planes; however, only $\langle a\rangle$-dislocations on basal planes (i.e., $(0001)\langle 11\bar{2}0\rangle$) and $\langle c+a\rangle$-dislocations on 2nd order pyramidal planes (i.e., $(11\bar{2}2)\langle 11\bar{2}3\rangle$) play the major role in either orientation. Furthermore, recent MD simulations also shows that $\langle c+a\rangle$-dislocations nucleate on 1st order pyramidal planes and then transition to 2nd order pyramidal planes through cross-slip or cooperative slip. Consequently, slip would subsequently occur predominantly on 2nd order pyramidal planes [112]. This agrees well with reports that only basal and 2nd order pyramidal slip were observed experimentally for both orientations [93–97]. Thus, in the following simulations, only these two types of dislocations were considered. The initial dislocation density prescribed on basal planes was 4×10^{12} m^{-2}, and on 2nd order pyramidal planes was 2×10^{12} m^{-2}.

A small degree of misorientaion (<10°) was typically reported for microcrystals oriented for c-axis compression [96,97]. This misorientaion is either pre-existent or develops during deformation due to crystallographic rotation resulting from a stiff loading axis that produces high friction forces between the microcrystal top-surface and the load platen [113,114]. To mimic this frictional stress effect, an increasing shear stress is applied on the top surface in the [0001] case. This shear stress is expressed as $\tau_{top} = \tau_{zx} = |\sigma| \tan(\theta_{mis})$, where σ is the applied axial stress, $\theta_{mis} = 10° \left(\varepsilon - \varepsilon_y\right)/\left(\varepsilon_{final} - \varepsilon_y\right)$ for $\varepsilon > \varepsilon_y$ is the misorientation angle, ε_y is the yielding strain, and ε_{final} is the final strain of 1.5%. Thus, the maximum misorientation angle will be 10° at the end of the simulations.

5.3 Results

5.3.1 Basal slip orientation: 22-69° tilted from {0001}

A SEM image of a representative sample with the diameter of 847 nm is shown in Figure 5.2b. The stress-strain data shown in Figure 5.2a exhibits several strain bursts typical of single crystalline micro-and nano-scale pillar compression tests [1,2]. The axial flow stress at the unloading strain of 16% is 107 MPa, which shows that negligible strain hardening occurred between yield at 115 MPa and unloading. The SEM image of this sample after the compression is shown in Figure 5.2b and reveals that the deformation commenced by a series of parallel shear offsets emanating from the top of the pillar.

In contrast, a 2125 nm-diameter sample yielded at 34 MPa and showed an increase in stress up to 86 MPa at the final unloading strain of 10%. The post-deformation image given in Figure 5.2c indicates that deformation was accommodated by a series of parallel shear offsets along the pillar.

An inclination of 48° between the loading direction and the c-axis in the 847 nm diameter sample shown in Figures 5.2b results in a critical resolved shear stress (CRSS), τ_{CRSS}, of 51 MPa; an inclination of 22° in the 2125 nm-diameter sample results in a CRSS of 11 MPa. These values are comparable to the range of CRSS of 39-68 MPa reported for the 3 µm diameter Mg single crystals compressed along the $[2\bar{3}14]$ direction [96]. For the 847 nm-diameter AZ31 sample studied in this work this represents an increase in CRSS by two orders of magnitude over the basal CRSS of Mg (~0.5 MPa) and 29 times the basal CRSS of Mg+0.45 at.% Zn (1.75 MPa) bulk single crystals [87,106]. The average elastic modulus was estimated to be 40.5±9.2 GPa and compares well to the average modulus of pure Mg (43.7 GPa) [115] and Mg + 4.5% Al + 1% Zn (44.6 GPa) [116] at similar tilt angles between 22-69° from the c-axis.

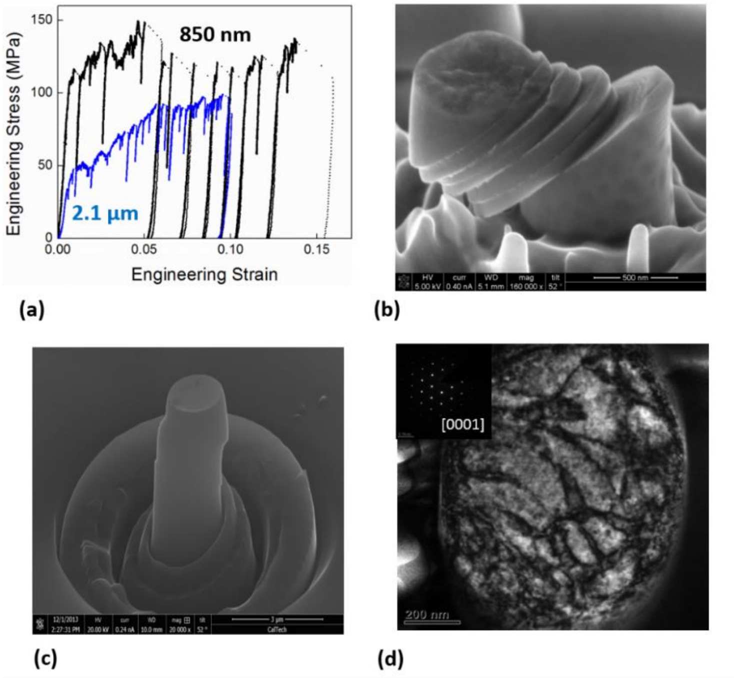

Figure 5.2: (a) TEM micrograph showing a porous oxide covering the AZ31 surface. This was observed during electro-polishing at elevated temperatures or if the sample was not immediately cleaned following polishing. The amorphous layer of Pt was used as protection during the TEM sample preparation process. (b) SEM image of the smoothed sample surface following electro-polishing. Al-Mg precipitates ranging approximately 1 to 10 µm can be seen partially and fully embedded in the AZ31 matrix. (c) Orientation Imaging Microscopy map generated by EBSD showing grain structure of annealed and polished surface with average grain size of 11.5±9.6 µm. (d) Stereographic triangle showing the grain orientations that were used to fabricate compression samples.

5.3.2 Pyramidal slip orientation: (0001)

The stress-strain data for a representative 840 nm-diameter pillar oriented for pyramidal slip is shown in Figure 5.3b. This sample yielded at an axial stress of 654 MPa, and the stress-strain data displayed similar strain bursts characteristic to basal slip-oriented samples shown in Figure 5.2a. The final stress at the unloading strain of 11.6% was 831 MPa, a value 27% higher than the yield stress. Figure 5.3c shows a SEM image of this sample after compression and reveals that the deformation was mostly homogeneous. The sample diameter widened from 840 nm to 940 nm and barreled. A small shear offset at midpoint of the cylinder oriented perpendicular to the loading axis was also observed. Micron-sized samples showed qualitatively similar stress-strain data.

The axial yield stress compares well to axial stresses of pure Mg micro-pillars with 630-685 nm diameter compressed along the c-axis of 600-680 MPa [96]. A misorientation from the c-axis of 2.2° corresponds to resolved shear stresses for 2nd order <a+c> pyramidal slip of 302 MPa. The average elastic modulus was 61.6±10.3 GPa compared to the modulus along the c-axis of 50.8 GPa in pure Mg [117].

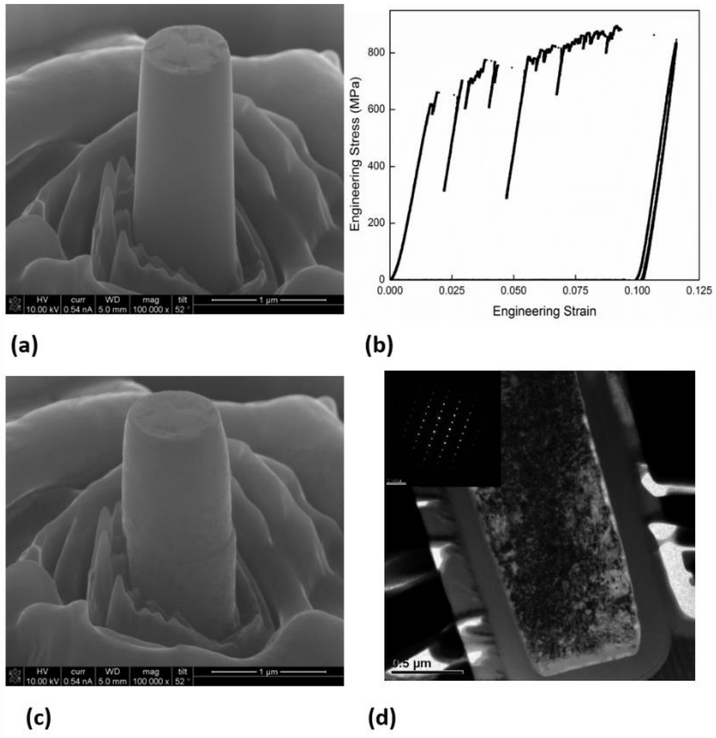

Figure 5.3: (a) Pre-deformation SEM image of 840 nm diameter sample nominally oriented for compression parallel to the *c*-axis. (b) Engineering stress–strain data for pyramidal sample displaying strain bursts and significant strain hardening. (c) Post-deformation SEM image showing deformation is mostly homogeneous. A single slip plane that is nearly perpendicular to the loading axis can be seen towards the bottom of the pillar. Samples greater than a micron in diameter failed by catastrophic strain bursts and so no comparison of the post-elastic behavior can be made to sub-micron samples. (d) Post-deformation TEM micrograph of a 860 nm-diameter *c*-axis sample. Diffraction contrast indicates a high dislocation density. The inset diffraction spot pattern shows that the sample is single crystalline.

5.3.3 Microstructure analysis

Figure 5.4a shows a bright field TEM micrograph that reveals several rod-like and circular second phase particles with the average diameters of 29 nm. A high-resolution TEM of one of these particles is shown in Figure 5.4b. Energy dispersive x-ray spectroscopy data shown in Figure 5.4c indicates that these phases are Mn rich, which is consistent with its dominance in the AZ31 composition at ~0.44% wt. These particles are most likely some form of Al-Mn intermetallic that has been predicted and observed in similar AZ alloys [118–120]. The precipitate areal density was estimated to 0.98% based on measuring the total area of secondary phases in the images and with spacing as great as ~675 nm. Stanford and Atwell observed a similar dispersion of particles in bulk AZ31, and Orowan hardening in tension of bulk AZ31 [119]. In compression, the authors reported insensitivity to the precipitates and pointed to the observed proliferation of twinning during compression and suggested that the volume fraction (~0.3%) of Al-Mn particles was not sufficient to impact the twinning stress.

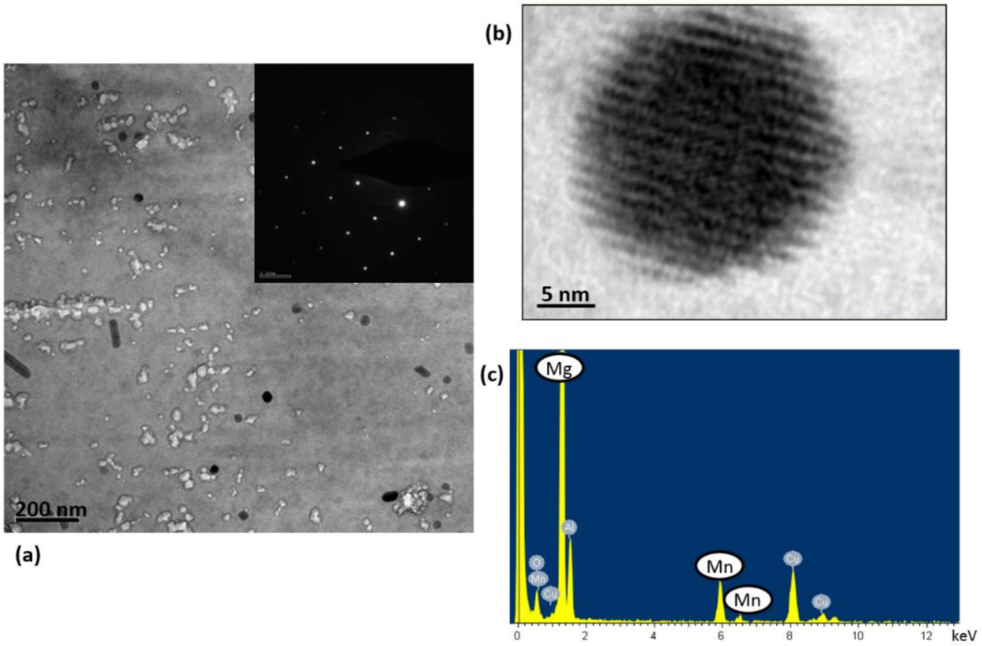

Figure 5.4: (a) TEM micrograph of bulk AZ31. Inset shows diffraction spot pattern for the image. Several cylindrical and spherical particles can be seen. The white foam-like structures are surface oxidation that began forming on the highly reactive Mg. (b) A HRTEM image of one of the particles of ~15 nm in diameter. Moiré fringes indicate the presence of a second phase. (c) EDS data reveals the particles to be Mn-rich. TEM images courtesy of Carol Garland.

5.3.4 Dislocation dynamics simulations

Figure 5.5a shows the engineering-stress versus engineering-strain response of [0001] and $[11\bar{2}2]$ oriented microcrystals having edge-length D = 1 μm. The yield stress of the [0001] oriented microcrystals is $\sigma_y \approx 270$ MPa (i.e., resolved shear stress $\tau_y = 121$ MPa), while the yield stress for the $[11\bar{2}2]$ oriented microcrystals is $\sigma_y \approx 50$ MPa (i.e., resolved shear stress $\tau_y = 25$ MPa). Qualitatively, [0001] microcrystals display a significant increase in stress following yield compared to $[11\bar{2}2]$ microcrystals. In Figure 5.5a, the variation of junction node number with applied strain is also plotted, and shows that more junction nodes appear in the [0001] orientated microcrystals than $[11\bar{2}2]$ ones. The *<a>*, *<c+a>*, and total dislocation densities for the two orientations are shown in Figure 5.5b. We can see that in the $[11\bar{2}2]$ case, only <a> dislocations on the basal plane contribute to the plastic deformation. However, in the [0001] microcrystals the *<c+a>* dislocation density increases after yield at ~0.45% strain. After 1% strain, the *<a>* dislocation density increases rapidly and exceeds the *<c+a>* dislocation density, indicating that basal slip occurs. This can also be seen in Figure 5.6, where the effective plastic strain map and deformation shape are shown. The [0001] orientated crystals without misorientation deform via multi-slip as shown in Figure 5.6b. However, under the shear stress from the simulated misorientation, acute basal slip can be seen in Figure 5.6a, although the Schmid factor on the basal slip planes is 0. Figure 5.6c shows the effective strain map of the $[11\bar{2}2]$ microcrystal, in which single-slip is clear. These simulations agree well with the current and previous experiment observations [96,97].

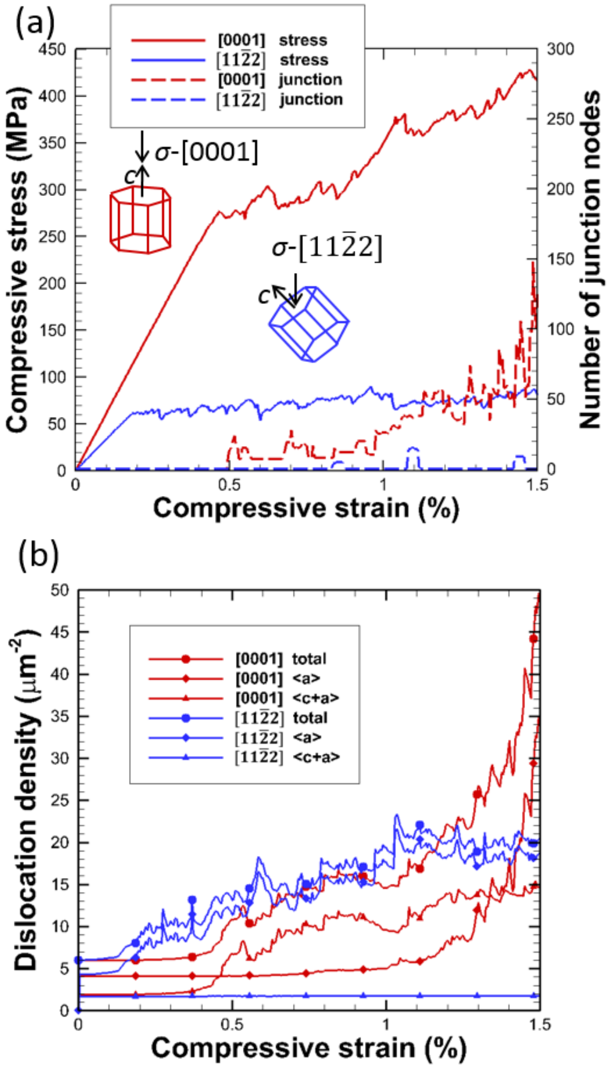

Figure 5.5: Figure 5. (a) Engineering-stress and number of junction nodes versus engineering-strain for microcrystals having 1 μm diameter and compressed along the [0001] (pyramidal slip) and $[11\bar{2}2]$ (basal slip) directions, respectively. Engineering stress is shown as solid lines and number of junction nodes is given by the dashed lines. (b) The total dislocation density, the ⟨*a*⟩ dislocation density on basal planes, and ⟨*c*+*a*⟩ dislocation density on the 2nd order pyramidal planes versus the axial engineering-strain.

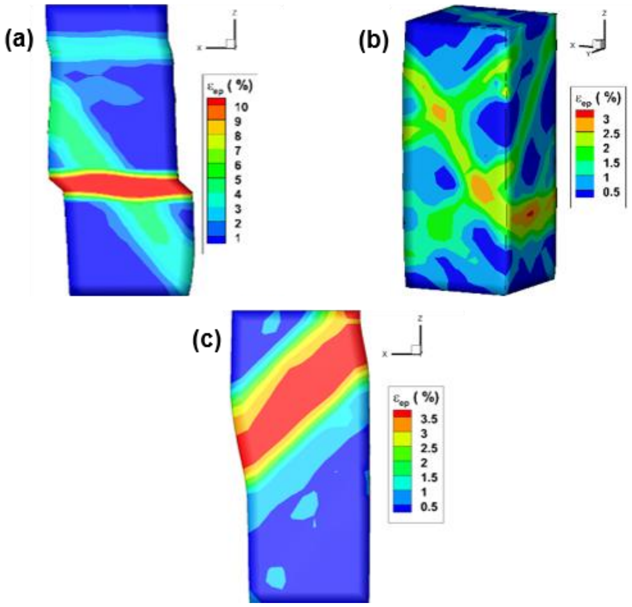

Figure 5.6: Figure 6. Effective plastic strain map and deformation shape at 1.5% strain for compression along: (a) $[0001]$ with 0-10° misorientation, (b) $[0001]$ without misorientation, and (c) $[11\bar{2}2]$ microcrystals. Note that the misorientation is achieved by applying shear stress on the top surface (see text). The displacement field in the *x* direction is magnified 5 times.

5.4 Effects of orientation

5.4.1 Basal slip orientation

The samples studied in this work were oriented such that the crystallographic direction parallel to the pillar axis was 22-69° away from the c-axis. This loading path applies a resolved shear stress onto the basal planes, which represent the weakest slip among Mg slip systems. Post-deformation SEM images of these samples fabricated from two separate grains, shown in Figures 5.2b and 5.2c, confirmed that the deformation was accommodated by shear on a single set of parallel slip planes. Figure 5.2d shows a TEM micrograph of the cross-section of one of these slip planes. The diffraction pattern shown in the inset reveals these slip planes are basal planes.

The strain bursts observed in the stress-strain signature of these samples that deformed via basal slip are similar to those in the micro- and nano-pillar compression experiments in FCC and BCC metallic single crystals. These bursts are often attributed to dislocation avalanches released from the pinning points that get activated as dislocation sources under applied stress [42,43]. Plastic deformation with a negligible change in the flow stress up to 15% axial strain suggests the deformation likely commenced on a single slip system, resulting in an “easy glide” plastic flow. Straining with little to no hardening has been observed in similar FCC micro- and nano-pillar compression experiments on samples loaded along both high and low-symmetry orientations [3,5,43,57]. In sub-micron samples, the annihilation of mobile dislocations at the free surface before they are able to multiply maintains this Stage I-like plastic behavior. In this regime, the probability of gliding dislocations interacting with one another and creating additional pinning points is lower than their propensity for annihilating at the free surface or at another existing sink. This mechanism is consistent with the observed lack of hardening and dislocation storage.

With increasing sample size, dislocations gliding in their slip planes will be increasingly more likely to encounter other dislocations or obstacles in their path before annihilation, which will cause interactions, pinning, and entanglement among them, thereby increasing dislocation density. Such dislocation multiplication can lead to back stresses and the shutdown of dislocation sources and will require a higher applied stress to propagate and to activate new, harder sources. This mechanism is consistent with a 90% increase in stress shown in Figure 5.2a for a 2125 nm sample. We found that all samples with diameters above 1 μm and oriented for basal slip showed this strain hardening-like behavior, a stress strain signature that has also been observed in micron-sized samples of pure Mg [94,96].

5.4.2 Pyramidal slip orientation

Compared to the samples oriented for basal slip, samples oriented for pyramidal slip attain substantially higher yield and flow stresses, as well as exhibit significant work hardening, as shown in Figure 5.3b. The c-axis has a high level of slip system symmetry with six 2nd order <a+c> pyramidal slip systems that have a Schmid factor of 0.447. Compression along such a high-symmetry orientation activates multiple non-parallel slip systems, which would lead to a relatively homogeneous deformation, non-localized deformation, a high degree of strain hardening, and high flow stresses, as also reported in similar experiments on pure single-crystalline Mg samples of equivalent dimensions [121,122]. SEM images of deformed samples in this study are given in Figure 5.3c, and reveal a 12% increase in average diameter from 840 nm to 940 nm.

Despite the activation of multiple non-parallel slip systems, the stress-strain data contains several strain bursts, similar to those observed in samples oriented for single-slip. The typical axial yield stress of 654 MPa for 840 nm diameter samples is more than twice that for basal samples. For such high axial stress, even a relatively low misalignment of 2.2° results in the maximum Schmid factor of 0.035 on the basal planes, which gives rise to the resolved basal stress of 29 MPa at unloading, on the order of critical shear stress in the samples that deformed by basal slip. A single slip plane approximately half-way down the compressed pillar height is shown in Figure 5.3c and conveys that it is nearly perpendicular to the c-axis, which suggests that even at low misalignment, basal slip is also activated during deformation, similar to deformation of pure Mg with low basal Schmid factors (0.035) [121]. In a small number of samples basal slip was activated and resulted in an instability, massive failure and early termination of the test (an example stress-strain plot is given in Figure S5.1), but the majority of samples could not have reached the high axial stresses as great as 831 MPa if basal slip was the dominant deformation mechanism. Furthermore, for the orientations of c-axis pillars tested, the greatest Schmid factor for prismatic slip ranges between 0.002-0.013 with an associated resolved shear stress at yield between 1.35-9.35 MPa. For the reported critical resolved shear stress of prismatic slip for Mg+0.45 at.% Zn bulk single crystals of 40.2 MPa [88], it is unlikely that prismatic slip has been activated at yield. The post-yield strain must be able to accommodate the applied deformation along the c-axis, which the <a> Burgers vectors of both the basal and prismatic slip systems will be unable to accommodate. The 1st and 2nd order pyramidal systems include <c+a> dislocations and are able to accommodate the imposed c-axis deformation. It is likely that the activation of multiple pyramidal slip systems accommodated most of the deformation, and that the mutual interactions of dislocations among these pyramidal systems, as well as between the pyramidal and basal planes, caused the observed work hardening.

For samples with diameters above 1 µm failure was often observed to occur by catastrophic bursts and so no comparison of the post-elastic behavior can be made to sub-micron samples.

We performed post-deformation TEM analysis of several c-axis samples and observed no clear evidence of twinning. Figure 5.3d shows a post-deformation TEM micrograph of an 860 nm-diameter c-axis pillar that was deformed to 4.8% engineering strain. The diffraction contrast indicates a high dislocation density and there is a lack of twinning boundaries. The inset diffraction spot pattern shows that the sample is single crystalline. This evidence along with the discussion in the previous paragraphs leads us to conclude that the dominant deformation mechanism in these samples was via pyramidal slip, in agreement with similar (pure Mg) micron-sized pillars compressed parallel to the c-axis [93,94,96]. These results are in contrast to the work of Yu, et al, in which pillars with diameters ranging from 150-200 nm in width with a rectangular cross-section displayed twin nucleation and twin propagation during [0001] compression, while nano-twin arrays formed during [0001] tension [99]. Easy activation of deformation twinning was also observed in bulk AZ31 compressed along the c-axis [123]. Although Al and Zn are typically expected to decrease the stacking fault energy of Mg [124], allowing for easier activation of twinning, we found pyramidal slip to be the prevalent deformation mechanism when compressed along the c-axis.

5.4.3 3D-DDD Simulations

Stress strain curves generated by 3D-DDD simulations showed several qualitative features also observed experimentally, including anisotropy in the yield stress of pillars oriented for basal or pyramidal slip, strain hardening of samples compressed along the [0001] direction, and activation of basal slip during [0001] compression with an induced misalignment.

Figure 5.5a shows a difference of 96 MPa between the CRSS of pillars in the $[11\bar{2}2]$ orientation and pillars in the [0001] orientation, an increase in yield stress qualitatively observed experimentally between pillars oriented for basal and pyramidal slip. To explain this anisotropy in the yield stress between both orientations, it is necessary to account for two competing effects, namely, the Peierls stress, τ_o, and the CRSS of the weakest dislocation sources, τ_s [125]. The resolved shear stress at yield for the [0001] orientation is observed to be on the order of the Peierls stress of *<c+a>* dislocations on 2nd order pyramidal planes. However, for the $[11\bar{2}2]$ orientation the resolved shear stress at yield is 50 times higher than the Peierls stress for *<a>* dislocations on the basal plane. According to the dislocation source model [5,42], the CRSS of a dislocation source having a mean length of 800b is τ_s = 24.5 MPa, which is considerably higher than the Peierls stress for *<a>* dislocations on the basal plane and considerably lower than that for *<c+a>* dislocations on 2nd order pyramidal planes. Thus, it may be concluded that the yield stress always satisfies the condition that τ_y is always on the order of the maximum of τ_s and τ_o.

The dislocation density evolution as a function of axial engineering-strain for microcrystals having edge length D = 1 µm in both orientations is shown in Figure 5.5b. It is observed that the dislocation activities are predominantly on 2nd order pyramidal planes for [0001] microcrystals, and predominantly on basal planes for $[11\bar{2}2]$ microcrystals. The Schmid factor on the basal plane is identically zero for loading along the [0001] direction. Thus, in the absence of any friction stresses on the top surface of the microcrystal, no major dislocation slip is expected on the basal planes and plasticity is mediated entirely by *<c+a>* dislocations slip. As a result, the [0001] microcrystals will deform in a multi-slip mode as shown in Figure 5.6b. On the other hand, while the maximum Schmid factor on the basal plane is 0.5 and on the 2nd order pyramidal planes is 0.3 for loading along the $[11\bar{2}2]$ direction, plasticity is mediated entirely by *<a>* dislocations slip on basal planes, since the Peierls stress of dislocations on the 2nd order pyramidal planes is 200 times higher than that for dislocations on the basal planes. This ensures that no dislocation slip on 2nd order pyramidal planes is expected, as shown in Figure 5.5b. Consequently, $[11\bar{2}2]$ oriented crystals will deform in a single slip mode, as shown in Figure 5.6c.

The [0001] microcrystals are observed to demonstrate a much stronger hardening response than $[11\bar{2}2]$ microcrystals. As discussed earlier, microcrystals with Schmid factors favorable for basal slip deform in a single slip mode and subsequently the number of junctions forming during deformation is considerably small (if any) as shown in Figure 5.5a. Thus, no forest hardening is expected, leading to a negligible hardening for the stress-strain curve. For [0001] microcrystals, dislocation activities are predominantly on 2nd order pyramidal planes. Unlike basal planes, 2nd order pyramidal planes intersect one another and there is a high chance for active dislocations to be trapped by other active dislocations lying on intersecting 2nd order pyramidal planes. Following the discussion of the [0001] compression experiments, this will lead to the shutdown of active sources and a higher stress is needed to activate new sources. In response, a stronger hardening is observed for [0001] microcrystals. This type of hardening has been first observed in FCC microcrystals and was termed “exhaustion hardening” [11].

In the case of an imposed shear stress on the top surface to mimic friction between the microcrystal top-surface and the indenter head, the resolved shear stress on the basal planes will constantly increase with increasing strain due to crystallographic rotations. At yield, $\theta_{mis} = 0°$, and the resolved shear stress of all 2nd order pyramidal planes is the same. Thus, the microcrystal will initially deform in a multi-slip mode. With increasing strain, θ_{mis} increases and the resolved shear stress on a single 2nd order pyramidal plane becomes higher than others, leading to slip predominately on that single plane as shown in Figure 5.6a. When θ_{mis} reaches ~5° (i.e., at a strain of 1% in the current simulations), the resolved shear stress on the basal plane becomes large enough to activate *<a>* dislocations. Once this occurs, basal slip dominates and the dislocation density of *<a>*-dislocation rapidly increases, as shown in Figures 5.5b. This behavior was also observed in [0001] compression experiments that displayed shear offsets nearly-perpendicular to the loading axis corresponding to the activation of basal slip, as shown in Figure 5.3c. In contrast to simulations, basal slip was not always the dominate deformation mechanisms observed experimentally with strain bursts seen accompanying stable hardening in these samples.

5.4 Size effects

Figure 5.7a shows the compressive yield stresses resolved onto the appropriate slip system as a function of sample diameter for each studied slip orientation in AZ31: (1) basal and (2) 2nd order pyramidal as well as resolved yield stresses at ε = 0.65%, as predicted from the current 3D-DDD simulations of Mg for compression along the $[11\bar{2}2]$ and [0001] directions. This plot conveys that the yield stress increases with decreasing pillar diameter for each orientation, similar to the well-known size effect in strength for FCC and BCC single crystalline metallic nano-sized samples [7,97].

Experimental results on pure Mg [95–97] are also shown for comparison. Specifically, Ye et al. [95] reported the resolved yield stresses for basal slip in pure Mg, Byer et al. reported the stress at 4% strain [96], and Kim reported the resolved shear stresses at 2% strain [97]. A clear power-law size-dependence of the form $\tau \propto D^{-n}$ is observed for all orientations. However, the power law exponent for samples oriented for basal slip (n = -1.11 from experiments and n = -1.44 from simulations) is considerably higher than that for samples compressed along the c-axis (n = -0.36 from experiments and n = -0.34 from simulations). Micropillar compression experiments on pure Mg also showed a decrease in strengthening exponent for samples that deformed by 2nd order pyramidal slip compared to basal slip [96,97]. The flow stresses of both slip systems in AZ31 and simulated $[11\bar{2}2]$ pillars are similar to those reported for pure Mg [95–97].The slight variation between the predicted power-law exponent and the stress levels from [0001] DDD simulations and experiments is due to differences in the initial dislocation densities [58], and/or the strain level at which the flow stress is computed [103]. The experimentally-measured dislocation density reported experimentally equal to 1.1×1013 m^{-2} [87], which is almost twice the density in the current DDD simulations.

While Figure 5.7a suggests that the microcrystal orientation plays a role in the extent of observed size-effects on the strength of the crystal, the underlying source leading to such orientation influence is still unknown. Schneider, et al. attributed different size effect intensities of FCC and BCC to the different Peierls stresses τ_o [126], which is strongly orientation dependent in HCP materials. According to the dislocation source model [13,126],

$$\tau_{CRSS} = \tau_o + \alpha \frac{Gb}{\bar{\lambda}_{max}}, \qquad \text{Eq. (5.6)}$$

we can see there are four important parameters: τ_o, G, b and $\bar{\lambda}_{max}$. The main size dependent parameter is the statistically maximum dislocation source length, $\bar{\lambda}_{max}$, while the other three are material properties and all orientation dependent due to material anisotropy. We can speculate that both the shear modulus, G, and the Burgers vector magnitude, b, contribute to the size dependence in addition to the Peierls stress, τ_o. In order to isolate such an effect due to anisotropy, we introduced an effective resolved shear stress per unit Burgers vector $\frac{\tau_{CRSS}-\tau_o}{Gb} = \frac{\alpha}{\bar{\lambda}_{max}}$ to see the orientation influence on $\frac{\alpha}{\bar{\lambda}_{max}}$. Figure 5.7b shows a clear power-law size-dependence for both orientations with the exponent being qualitatively the same. This suggests that the effect of orientation on size-induced strengthening shown in Figure 5.7a is from the material anisotropy, which is characterized by τ_o, G, b [11,125].

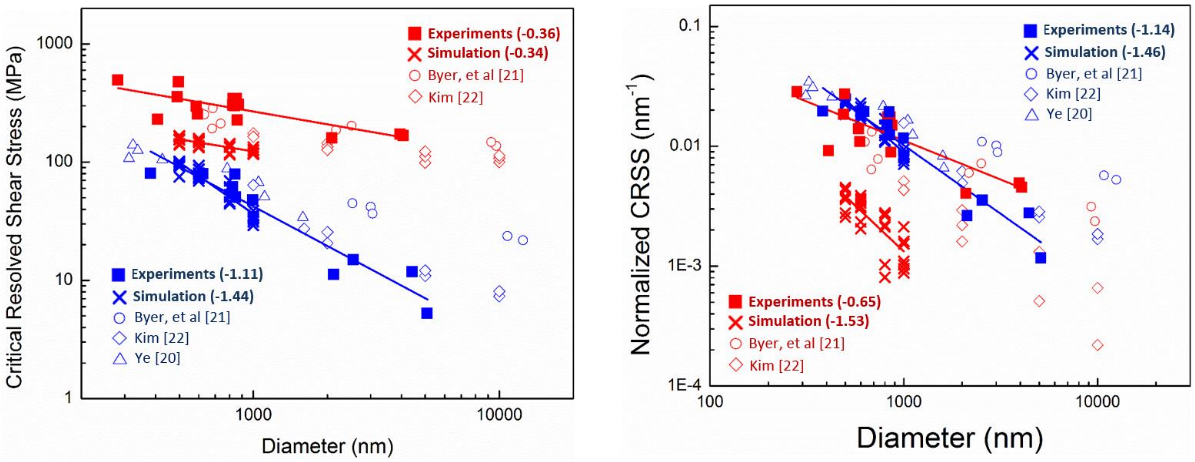

(a) **(b)**

Figure 5.7: (a) CRSS for compression samples oriented for basal (blue) and pyramidal (red) slip plot versus sample diameter. Power-law exponents are given in parenthesis for both experiments and simulations. Included are reported yield strengths for similar micro- and nano-pillar compression experiments on pure Mg. The alloy pillars show a greater rate of strengthening than pure Mg. Both sets of experimental samples and simulation of $[11\bar{2}2]$ compression show similar yield strengths to pure Mg. (b) The effective resolved shear stress per unit burgers vector plot versus sample diameter for the same set of data shown in (a). All data except simulated [0001] compression is seen to collapse, showing that the size effect is the same for both basal and pyramidal slip.

To investigate the influence of orientation on the microstructural contribution to the size effect, we analyzed the microstructure evolution generated through the present DDD simulations. Figure 5.8 shows the superposition of several snapshots of dislocation microstructures separated by 0.2% strain intervals after yielding, in which the dislocation slip traces can be seen. Figure 5.8a conveys that almost all <*c+a*> dislocation sources were activated after yielding in the [0001] oriented microcrystals since the Schmid factor is the same on all planes. For $[11\bar{2}2]$ oriented microcrystals, Figure 5.8b shows many <a> sources that were not activated. The figure also shows the presence of multiple straight screw dislocation segments. This dislocation evolution is likely a result of the low mobility of screw dislocations. In the case of $[11\bar{2}2]$ orientation <*a*> dislocation having Burgers vector in the $[11\bar{2}0]$ direction are easily activated since their Schmid factor is higher than <*a*> dislocations with the Burgers vectors parallel to $[1\bar{2}10]$ and $[\bar{2}110]$. As a result, about half of the dislocation sources on the basal plane can contribute to plastic deformation during $[11\bar{2}2]$ loading. Thus, in the current DDD simulations, while the initial dislocation density on the basal plane is twice than that on 2nd order pyramidal planes, the number of activated dislocation sources on the basal plane is almost the same as the number of sources on the 2nd order pyramidal plane. This might explain why there is no orientation influence on the size effects, as shown in Figure 5.7b.

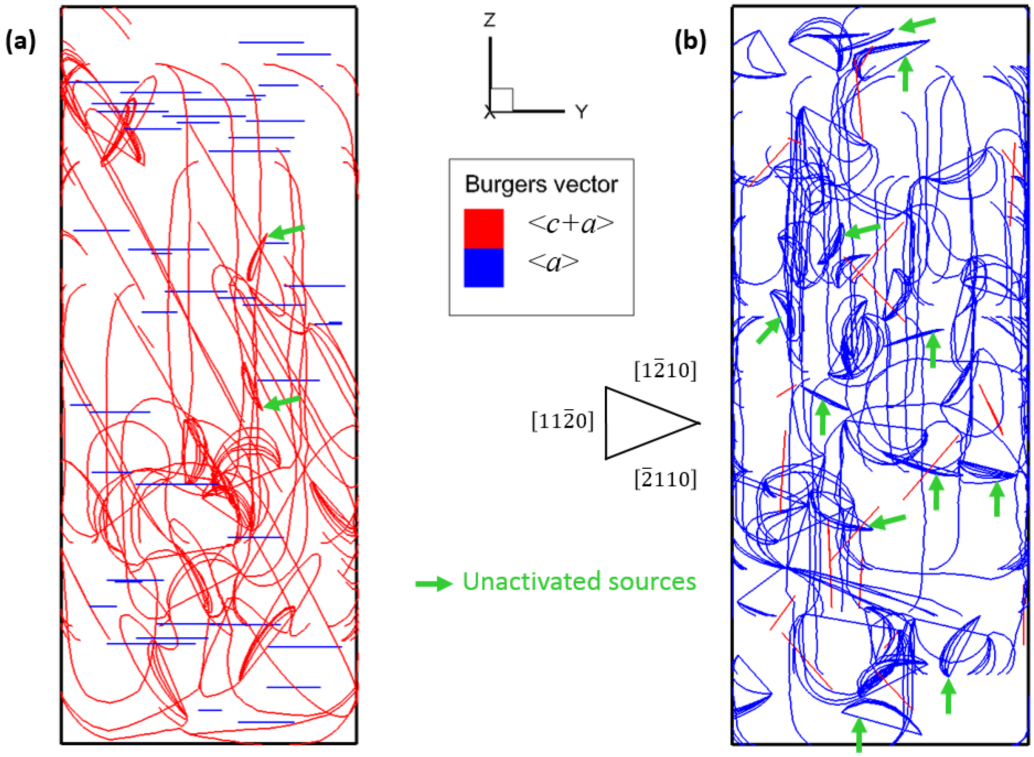

Figure 5.8: Dislocation microstructure evolution shown sequentially for (a) [0001] microcrystals between 0% and 0.6% strain and (b) $[11\bar{2}2]$ microcrystals between 0%, and 0.4%. The notation of the <*a*> $< 11\bar{2}0 >$ dislocations is used in (b).

5.4 Dispersion and solute effects

All previous experimental data on AZ31 has been reported for polycrystalline samples, making it difficult to separate the alloying effect on the strength from other microstructural effects. Akhtar and Teghtsoonian studied the CRSS for basal slip in several bulk single crystalline binary Mg alloys in tension [87,88,127]. These authors observed a CRSS of 2.9 MPa for basal slip in dilute Mg alloys with ~1.63 at.% Al and of 1.75 MPa in alloys with ~0.45% at.% Zn. These stresses are a factor of 3 higher than 0.5 MPa reported for basal slip in pure Mg [87,127] under similar processing treatments. They noted that for dilute concentrations, the increase in stress caused by solid solution strengthening was proportional to $c^{2/3}$, where c is the atomic concentration of solute. Yasi, et al. used first principles computations to calculate the strengthening effect for slip in pure Mg across the basal plane by introducing solute particles of varying element [128]. Based on these calculations, we would expect a total solid-solution strengthening effect in AZ31 to be on the order of ~5 MPa. This predicted solid solution strengthening in bulk is much less than the predicted increase in flow stress due to the size effect.

The effect of secondary phases on the strength of nano-sized metallic samples has not been extensively studied. The yield strength was reported to be independent of pillar size in a Ni-based alloy (Inconel MA6000) that contained 20-30 nm diameter Y_2O_3 particles spaced less than 100 nm apart [129]. The length-scale of particle spacing dominated the sample size and so they observed bulk-like behavior. Fe nanopillars with low initial dislocation densities that contained Nb clusters exhibited a slight increase in strength of ~ 0.11 GPa, as compared to pure Fe nanopillars, but this was considered statistically insignificant compared to the overall strength of 2 GPa [130]. These authors concluded that the strengthening was governed by intrinsic properties and not by the presence of precipitates.

The spacing of 2nd phases observed in this work was as great as 675 nm, greater than the radius of most compression samples, and so we would expect the stress required to activate single-arm sources to be on the order or greater than the bowing stress. Figure 5.7a clearly shows that there is no significant contribution to the yield stress from the presence of 2nd phases as the alloy shows similar yield stresses as Mg. Sub-micron samples show a post-elastic insensitivity to the presence of 2nd phases, but further study is required to determine whether they contribute to the rate of hardening in the 2 and 5 µm diameter samples.

5.5 Summary

We investigated the mechanical response of AZ31 nanopillars compressed along two crystallographic directions: (1) parallel to the (0001) direction, nominally oriented for basal slip and (2) misoriented from the c-axis by 22-69°. We also employed 3D-DDD simulations for pure Mg pillars under $[11\bar{2}2]$ and [0001] compressive loading. For samples nominally oriented for basal slip, we observed stress-strain behavior indicative of single-slip deformation and strain bursts typical of nano-compression experiments. DDD simulations revealed weak dislocation interactions resulting in weak hardening and single slip. Samples compressed along the c-axis displayed both strain bursts and significant hardening in their stress-strain data. DDD simulations showed a pronounced increase in junction formation due to the activation of multiple intersecting slip systems. Yield strengths in these samples were approximately twice as great as basal samples and were high enough to activate basal slip even for small misalignments away from the c-axis. There is a clear size effect seen in each set of samples, the yield strength increasing with decreasing pillar diameter. The size effect followed a power-law with differing exponent for each system that was shown to be a result of the underlying anisotropic intrinsic lattice resistance. The power-law exponent for basal slip was -1.11 for experiments and -1.44 for simulations, while the exponent for samples compressed along the c-axis was -0.36 for experiments and -0.34 for simulations. By accounting for the anisotropic material properties through the effective resolved shear stress per unit burgers vector, this anisotropy disappeared, showing that the mechanism of the size effect is the same in both orientations. Yield strengths in the AZ31 alloy were similar to Mg in both orientations, showing that at this length scale, the size effect overrides solid solution strengthening and that the yield strength is insensitive to the presence of second phases.

6. Conclusions and Outlook

This work has considered the mechanical effects of a variety of manifestations of interfaces within nano-scale metals. We first considered the emergence of hysteresis loops in Cu nanopillars coated with an Al_2O_2 coating. We then considered the mechanical effect of an internal boundary through compression of Al nanopillars containing a vertically-aligned CSL grain boundary. These high-symmetry boundaries showed no apparent impact on either the mechanical properties of on dislocation migration. By fabricated compression samples that contained a high-angle grain boundary at an angle tilted away from the loading axis, we were able to then investigate the effect of grain boundary stress state on the dominate deformation mechanisms. We observed a transition from dislocation-dominated plasticity to deformation by room temperature grain boundary sliding with increased shear applied across the grain boundary. We then finished by investigating the role of crystal structure and alloying on the mechanical properties of a Mg alloy and observed that the size effect dominated any alloying effect and that differences in the size effect based on crystal orientation was a result of the inherent crystal anisotropy.

Some general conclusions that can be drawn from these studies are that the loading orientation plays an important role on the dominate deformation mechanism within these nano-scale metals. The increased activation stress due to the effect of sample size allows for competition between dislocation-mediated plasticity and grain boundary sliding at room temperature. A wider range of tilt angles should be studied to investigate at what stress state a transition between these two mechanisms occurs.

Within samples that deform via grain boundary sliding, it has been shown here that the difference between the loading rate and the rate of grain boundary sliding results in qualitative features observed in the stress-strain data. These features resembles the behavior of a frictional, damped harmonic system and suggest that investigation through a range may reveal a variety of stress-strain responses. It would be of interest to investigate this deformation at a variety of loading rates that would represent both underdamped and overdamped systems. These are both open questions that can be answered using the methods described in this work.

Within samples that deform via nucleation and migration of dislocations, we have shown that high-symmetry CSL grain boundaries do not significantly interact with dislocation migration. There is an opportunity to expand this study to include a wider range of CSL-type boundaries to less-symmetric, but still coincident boundaries. The well-characterized atomic configuration of these CSL boundaries allows this investigation to be more easily undertaken through methods of molecular dynamics simulations. Other avenues of include the development of cold-welding or electrodeposition techniques that may allow for better fabrication of specific grain orientations and thus known grain boundary types. This would allow for higher-throughput experimental fabrication and mechanical testing. In the work presented here on the effects of alloying, we have studied a limited range of alloy concentration and element. Through comparison to pure Mg, we have observed no effect on the yielding behavior in nanoscale AZ31 at the concentrations studied here. TEM analysis reveals that the density of secondary phases may not have an effect on the dislocation source length. With increasing secondary phase density, we would expect a competition between the current single-arm sources and secondary phases as Frank-Read sources. This can be investigated through application of the techniques discussed here on a wider range of Mg alloys and alloy concentrations.

Investigation into the effects of microstructural interfaces on the mechanical behavior of nano-scale metals covers an immense number of increasingly-complex microstructures. We have considered several of these microstructures here, but have also outlined several open questions and avenues of investigation. We hope this thesis will serve as a guide and reference for future work.

Bibliography

[1] Greer JR, De Hosson JTM. Prog Mater Sci 2011;56:654.

[2] Uchic MD, Shade P a., Dimiduk DM. Annu Rev Mater Res 2009;39:361.

[3] Dimiduk D, Uchic MD, Parthasarathy TA. Acta Mater 2005;53:4065.

[4] Rao SI, Dimiduk DM, Tang M, Uchic MD, Parthasarathy TA, Woodward C. Philos Mag 2007;87:4777.

[5] Greer JR, Nix WD. Phys Rev B 2006;73:1.

[6] Gu XW, Loynachan CN, Wu Z, Zhang YW, Srolovitz DJ, Greer JR. Nano Lett 2012;12:6385.

[7] Uchic MD, Dimiduk DM, Florando JN, Nix WD. Science 2004;305:986.

[8] Greer JR, Oliver WC, Nix WD. Acta Mater 2005;53:1821.

[9] Lee S-W, Han SM, Nix WD. Acta Mater 2009;57:4404.

[10] Schneider AS, Kiener D, Yakacki CM, Maier HJ, Gruber PA, Tamura N, Kunz M, Minor AM, Frick CP. Mater Sci Eng A 2013;559:147.

[11] Rao SI, Dimiduk DM, Parthasarathy TA, Uchic MD, Tang M, Woodward C. Acta Mater 2008;56:3245.

[12] Hirth JP, Lothe J. Theory of Dislocations, Second Edi. New York: John Wiley & Sons, Inc.; 1982.

[13] Parthasarathy T a., Rao SI, Dimiduk DM, Uchic MD, Trinkle DR. Scr Mater 2007;56:313.

[14] Oh SH, Legros M, Kiener D, Dehm G. Nat Mater 2009;8:95.

[15] Jennings AT, Li J, Greer JR. Acta Mater 2011;59:5627.

[16] Nicola L, Xiang Y, Vlassak JJ, Van der Giessen E, Needleman A. J Mech Phys Solids 2006;54:2089.

[17] Xiang Y, Vlassak JJ. Acta Mater 2006;54:5449.

[18] Xiang Y, Vlassak JJ. Scr Mater 2005;53:177.

[19] Ng KS, Ngan AHW. Acta Mater 2009;57:4902.

[20] Greer JR. Effective Use of Focused Ion Beam (FIB) in Investigating Fundamental Mechanical Properties of Metals at the Sub-Micron Scale, in:. Mater. Res. Soc. Symp. Proc. 2006.

[21] Jennings AT, Gross C, Greer F, Aitken ZH, Lee SW, Weinberger CR, Greer JR. Acta Mater 2012;60:3444.

[22] Jennings AT, Burek MJ, Greer JR. Phys Rev Lett 2010;104:135503.

[23] El-Awady JA, Rao SI, Woodward C, Dimiduk DM, Uchic MD. Int J Plast 2011;27:372.

[24] Zhou C, Biner S, Lesar R. Scr Mater 2010;63:1096.

[25] Nicola L, Van der Giessen E, Needleman A. J Appl Phys 2003;93:5920.

[26] Rao SI, Hazzledine PM. Philos Mag A 2000;80:2011.

[27] Koehler JS. Phys Rev B 1970;2:547.

[28] Guruprasad PJ, Carter WJ, Benzerga AA. Acta Mater 2008;56:5477.

[29] Mara NA, Bhattacharyya D, Dickerson P, Hoagland RG, Misra A. Appl Phys Lett 2008;92:231901.

[30] Li N, Mara NA, Wang YQ, Nastasi M, Misra A. Scr Mater 2011;64:974.

[31] Jang D, Li X, Gao H, Greer JR. Nat Nanotechnol 2012;7:594.

[32] Jang D, Cai C, Greer JR. Nano Lett 2011;11:1743.

[33] Jang D, Greer JR. Scr Mater 2011;64:77.

[34] Ng KS, Ngan AHW. Philos Mag 2009;89:3013.

[35] Kunz A, Pathak S, Greer JR. Acta Mater 2011;59:4416.

[36] Kheradmand N, Dake J, Barnoush A, Vehoff H. Philos Mag 2012;92:3216.

[37] Sutton AP, Balluffi RW. Interfaces in Crystalline Materials. Oxford University Press; 1995.

[38] Tucker GJ, Aitken ZH, Greer JR, Weinberger CR. Model Simul Mater Sci Eng 2013;21:015004.

[39] Hirouchi T, Shibutani Y. Mater Trans 2014;55:52.

[40] Imrich PJ, Kirchlechner C, Motz C, Dehm G. Acta Mater 2014;73:240.

[41] Dimiduk DM, Woodward C, Lesar R, Uchic MD. Science 2006;312:1188.

[42] Ng K, Ngan A. Acta Mater 2008;56:1712.

[43] Brinckmann S, Kim J-Y, Greer J. Phys Rev Lett 2008;100:155502.

[44] Mishin Y, Farkas D, Mehl M, Papaconstantopoulos D. Phys Rev B 1999;59:3393.

[45] Plimpton S. J Comp Phys 1995;117:1.

[46] Li J. Model Simul Mater Sci Eng 2003;11:173.

[47] Stukowski A. Model Simul Mater Sci Eng 2009;18:015012.

[48] Kelchner C, Plimpton S, Hamilton J. Phys Rev B 1998;58:11085.

[49] Faken D, Jónsson H. Comput Mater Sci 1994;2:279.

[50] Tsuzuki H, Branicio PS, Rino JP. Comput Phys Commun 2007;177:518.

[51] Liu C-L, Plimpton SJ. J Mater Res 1995;10:1589.

[52] Kegg GR, Horton CAP, Silcock JM. Philos Mag 1973;27:1041.

[53] Fukutomi H, Kamijo T. Scr Metall 1985;19:195.

[54] Babcock S., Balluffi R. Acta Metall 1989;37:2357.

[55] Jang D, Gross CT, Greer JR. Int J Plast 2011;27:858.

[56] Nix WD, Lee S-W. Philos Mag 2011;91:1084.

[57] Volkert C a., Lilleodden ET. Philos Mag 2006;86:5567.

[58] Shan ZW, Mishra RK, Syed Asif S, Warren OL, Minor AM. Nat Mater 2008;7:115.

[59] Friedman N, Jennings AT, Tsekenis G, Kim JY, Tao M, Uhl JT, Greer JR, Dahmen KA. Phys Rev Lett 2012;109.

[60] Fukutomi H, Iseki T, Endo T, Kamijo T. Acta Metall Mater 1991;39:1445.

[61] King AH, Smith DA. Acta Crystallogr Sect A 1980;36:335.

[62] Farkas D. J Phys Condens Matter 2000;12:R497.

[63] Sansoz F, Molinari JF. Acta Mater 2005;53:1931.

[64] Molteni C, Marzari N, Payne M, Heine V. Phys Rev Lett 1997;79:869.

[65] Du N, Qi Y, Krajewski PE, Bower AF. Acta Mater 2010;58:4245.

[66] Pereiro-López E, Ludwig W, Bellet D, Lemaignan C. Acta Mater 2006;54:4307.

[67] Schmid S, Sigle W, Gust W, Ruhle M. Zeitschrift für Met 2002;93:428.

[68] Itoh a, Izumi J, Ina K, Koizumi H. J Phys Conf Ser 2010;240:012033.

[69] Hugo RC, Hoagland RG. Acta Mater 2000;48:1949.

[70] Thomson DI, Heine V, Payne MC, Marzari N, Finnis MW. Acta Mater 2000;48:3623.

[71] Kiener D, Motz C, Rester M, Jenko M, Dehm G. 2007;459:262.

[72] Greer JR, Espinosa H, Ramesh KT, Nadgorny E. Appl Phys Lett 2008;92.

[73] Dehm G. n.d.

[74] Griffith AA. Philos Trans R Soc A Math Phys Eng Sci 1921;221:163.

[75] Olmsted DL, Foiles SM, Holm EA. Acta Mater 2009;57:3694.

[76] Tyson WR, Miller WA. Surf Sci 1977;62:267.

[77] Jennings AT, Weinberger CR, Lee SW, Aitken ZH, Meza L, Greer JR. Acta Mater 2013;61:2244.

[78] Dix EH. SAE Tech Pap 1929:498.

[79] Archbutt SL, Jenkin JW. Nature 1922;109:251.

[80] Luo A. JOM 2002;54:42.

[81] Staiger MP, Pietak AM, Huadmai J, Dias G. Biomaterials 2006;27:1728.

[82] Kulekci MK. Int J Adv Manuf Technol 2007;39:851.

[83] Zeng R, Dietzel W, Witte F, Hort N, Blawert C. Adv Eng Mater 2008;10:B3.

[84] Ogarevic VV, Stephens RI. Annu Rev Mater Sci 1990;20:141.

[85] Mordlike BL, Ebert T. Mater Sci Eng A 2001;302:37.

[86] Mises R V. ZAMM - Zeitschrift für Angew Math und Mech 1928;8:161.

[87] Akhtar A, Teghtsoonian E. Acta Metall 1969;17:1339.

[88] Akhtar A, Teghtsoonian E. Acta Metall 1969;17:1351.

[89] Bohlen J, Nürnberg MR, Senn JW, Letzig D, Agnew SR. Acta Mater 2007;55:2101.

[90] Barnett MR, Keshavarz Z, Beer a G, Atwell D. Acta Mater 2004;52:5093.

[91] Ding SX, Lee WT, Chang CP, Chang LW, Kao PW. Scr Mater 2008;59:1006.

[92] El-Awady JA, Uchic MD, Shade PA, Kim S-L, Rao SI, Dimiduk DM, Woodward C. Scr Mater 2013;68:207.

[93] Byer CM, Li B, Cao B, Ramesh KT. Scr Mater 2010;62:536.

[94] Lilleodden E. Scr Mater 2010;62:532.

[95] Ye J, Mishra RK, Sachdev AK, Minor AM. Scr Mater 2011;64:292.

[96] Byer CM, Ramesh KT. Acta Mater 2013;61:3808.

[97] Kim GS. Small Volume Investigation of Slip and Twinning in Magnesium Single Crystals. 2011.

[98] Kim GS, Yi S, Huang Y, Lilleodden E. MRS Proc 2011;1224:1224.

[99] Yu Q, Qi L, Chen K, Mishra RK, Li J, Minor AM. Nano Lett 2012;12:887.

[100] Zbib HM, Diaz de la Rubia T. Int J Plast 2002;18:1133.

[101] Zbib HM, Rhee M, Hirth JP. Int J Mech Sci 1998;40:113.

[102] Pérez-Prado MT, Ruano O a. Scr Mater 2002;46:149.

[103] Wang Y., Huang J. Mater Chem Phys 2003;81:11.

[104] Partridge PG. Int Mater Rev 1967;12:169.

[105] Balasubramanian S, Anand L. Acta Mater 2002;50:133.

[106] Conrad H, Robertson WD. Trans Metall Soc Aime 1957;209:503.

[107] Reed-Hill R., Robertson W. Acta Metall 1957;5:717.

[108] Staroselsky A, Anand L. Int J Plast 2003;19:1843.

[109] Groh S, Marin EB, Horstemeyer MF, Bammann DJ. Model Simul Mater Sci Eng 2009;17:075009.

[110] Tang Y, El-Awady JA. Mater Sci Eng A 2014;618:424.

[111] Fan H, Li Z, Huang M. Scr Mater 2012;66:813.

[112] Tang Y, El-Awady JA. Acta Mater 2014;71:319.

[113] Kuroda M. Acta Mater 2013;61:2283.

[114] Shade PA, Wheeler R, Choi YS, Uchic MD, Dimiduk DM, Fraser HL. Acta Mater 2009;57:4580.

[115] Hearmon RF. The Elastic Constants of Crystals and Other Anisoptropic Materials. Berlin: Springer-Verlag; 1979.

[116] Nikishin a. V., Nikolaev DI. Crystallogr Reports 2008;53:493.

[117] Tromans D. Dep Mater Eng Univ … 2011;6:462.

[118] Masoumi M, Zarandi F, Pekguleryuz M. Mater Sci … 2011;528:1268.

[119] Stanford N, Atwell D. Metall Mater Trans A 2013;44:4830.

[120] Nakaura Y, Watanabe A, Ohori K. Mater Trans 2006;47:1743.

[121] Obara T, Yoshinga H, Morozumi S. Acta Metall 1973;21.

[122] Yoshinaga H, Horiuchi R. Trans JIM 1963;4:1.

[123] Barnett MR. Mater Sci Eng A 2007;464:1.

[124] Wang C, Zhang H-Y, Wang H-Y, Liu G-J, Jiang Q-C. Scr Mater 2013;69:445.

[125] El-Awady JA, Wen M, Ghoniem NM. J Mech Phys Solids 2009;57:32.

[126] Schneider AS, Frick CP, Clark BG, Gruber PA, Arzt E. Mater Sci Eng A 2011;528:1540.

[127] Akhtar A, Teghtsoonian E. Philos Mag 1972;25:897.

[128] Yasi J a., Hector LG, Trinkle DR. Acta Mater 2010;58:5704.

[129] Girault B, Schneider AS, Frick CP, Arzt E. Adv Eng Mater 2010;12:385.

[130] Xie KY, Shrestha S, Cao Y, Felfer PJ, Wang Y, Liao X, Cairney JM, Ringer SP. Acta Mater 2013;61:439.